Metamorphic evolution of the Great Slave Lake shear zone

Brendan Dyck[1]*, Rellie M. Goddard[2], David Wallis[3]†, Lars N. Hansen[4], Edith Martel[5]

[1]Department of Earth Sciences, Simon Fraser University, University Drive, Burnaby, BC V5A 1S6, Canada

[2]Department of Earth Sciences, Oxford University, South Parks Road, Oxford OX1 3AN, UK

[3]Department of Earth Sciences, Utrecht University, 3584 CB Utrecht, The Netherlands

[4]Department of Earth and Environmental Sciences, University of Minnesota, Minneapolis, Minnesota 55455, USA

[5]Northwest Territories Geological Survey, 4601-B 52 Avenue, Yellowknife, NWT X1A 1KS, Canada

*(brendan_dyck@sfu.ca)

†Now at: Department of Earth Sciences, University of Cambridge, Downing Street, Cambridge CB2 3EQ, UK

Running title: "Metamorphic evolution of the GSLsz"

ABSTRACT

The Paleoproterozoic Great Slave Lake shear zone (GSLsz) is a crustal-scale strike-slip structure, with a total length >1000 km and a width of ~25 km, that separates the Archean Rae and Slave cratons. The range of metamorphic rocks now exposed at the surface encompasses granulite facies mylonite through to lower-greenschist facies ultramylonite and cataclasite, providing a potential type example of fault-zone structure in the middle and lower crust. However, the metamorphic evolution of the units remains poorly quantified, hindering detailed structural and tectonic interpretations. Here, we use phase equilibria modelling and thermobarometry to determine the metamorphic conditions recorded by pelitic, mafic, and felsic GSLsz mylonites. Samples from the entire range of granulite–greenschist facies units preserve evidence for nested clockwise pressure–temperature paths that are consistent with a single orogenic cycle. Our findings indicate that the northern Rae margin underwent pervasive crustal thickening with peak pressures in metasedimentary rocks reaching ~1.1 GPa. The crustal thermal gradient at the onset of thickening was ~650ºC·GPa^{-1}, whereas, the final stages of equilibrium recorded by fine-grained matrix minerals in all samples collectively define a metamorphic field gradient of ~1000ºC·GPa^{-1}. Deformation microstructures are consistent with the main phase of dextral shear having been synchronous with or following peak metamorphism. The history of metamorphism and exhumation of the GSLsz is consistent with the Sibson-Scholz model for shear zones, with a narrowing of the deforming zone and the progressive overprinting of higher-grade assemblages during exhumation through shallower crustal levels.

1 INTRODUCTION

Characterization of the structural and petrological evolution of plate-boundary fault zones (*sensu lato*, including both upper crustal faults and their underlying shear zones) is central to modelling the occurrence (or absence) of plate tectonics. Observations of both active and ancient fault zones are typically interpreted in the context of the Sibson-Scholz model of fault-zone structure (Sibson, 1977, 1983; Scholz, 1988). In this model, increases in pressure and temperature with depth induce a transition from dominantly pressure-sensitive frictional failure in the upper crust to dominantly temperature-sensitive viscous flow in the lower crust, with a concomitant transition from narrow brittle faults to broad ductile shear zones. However, close examination of individual structures has revealed several complicating effects, including exhumation and/or burial during fault activity (e.g., Toy, Prior, & Norris, 2008; Parsons, Law, Lloyd, Phillips, & Searle, 2016), progressive fault-zone weakening (e.g., Holdsworth, 2004; Imber, Holdsworth, Smith, Jefferies, & Collettini, 2008; Wallis, Phillips, & Lloyd, 2013), and reactivation (potentially with different kinematics) during distinct tectonic events (e.g., Holdsworth et al., 1997, 2001). These effects are most prevalent in the continental lithosphere due to its longevity and structural complexity. As such, it is important to identify and characterize those continental fault zones that may pertain most closely to the basic Sibson-Scholz model to provide comparators against which to develop more complex models.

The Great Slave Lake shear zone (GSLsz) is a potential type example of a deeply eroded continental transform plate boundary. Early studies of the GSLsz helped to establish the current paradigm for the structure of major fault zones in the continental crust (Hanmer & Lucas, 1985; Hoffman, 1987; Hanmer, 1988, 1997). Importantly, the central portion of the GSLsz runs through homogeneous felsic intrusive lithologies that allow the effects of deformation conditions on fault-zone structure to be isolated, whilst mafic and pelitic enclaves are convenient for

providing geothermobarometric constraints (Hanmer, 1988; Hanmer, Bowring, van Breemen, & Parrish, 1992). Previous workers identified mylonitic units, with distinct metamorphic mineral assemblages, that exhibit broadly similar/compatible kinematic indicators and occur in an overprinting sequence of decreasing width, decreasing metamorphic grade, and increasing intensity of deformation fabrics (e.g., grain size reduction, foliation development) (Hanmer, 1988; Hanmer et al., 1992). The mylonitic units with the lowest metamorphic grades are partially overprinted by brittle fault rocks (Hanmer, 1988). These characteristics are consistent with the Sibson-Scholz model of fault zone structure, that was initially developed for fault zones dominated by a reverse component, and thereby began to establish the relevance of the model to major strike-slip structures (Hanmer, 1988).

Despite their significance for models of continental fault-zone structure, estimates of the metamorphic conditions recorded by each unit within the GSLsz have been based on sparse quantitative constraints (Hanmer, 1988). The lack of modern metamorphic studies on the GSLsz has left open questions regarding whether or not the laterally exposed metamorphic units reflect the vertical structure of a long-lived strike-slip fault zone. An alternative hypothesis is that the structure could have been reactivated at different crustal levels during temporally distinct deformation events. This latter model has been associated with several other major fault zones (e.g., Holdsworth et al., 1997, 2001). In this contribution, we use phase equilibria modelling and thermobarometry to constrain pressure–temperature (P–T) paths for the four main metamorphic units of the GSLsz. The improved P–T constraints provided here are a significant development in discriminating between the competing hypotheses. The conditions of final equilibration, which fall on a single metamorphic field gradient despite spanning greenschist- to granulite-facies

conditions are consistent with all the mylonitic units having formed during a single orogenic cycle in a single overarching structure.

2 GEOLOGICAL CONTEXT

Northern Laurentia is an amalgam of the Archean Slave, Rae, Hearne, and Superior cratons, all of which are separated by Paleoproterozoic belts that have unique magmatic, metamorphic, and deformation histories (Hoffman, 1988). The tectonic boundary between the Slave and Rae cratons forms one of these Paleoproterozoic belts and is itself divided, from north to south, into the Thelon Tectonic Zone (TTZ), Great Slave Lake shear zone (GSLsz), and the Taltson Magmatic Zone (TMZ; Fig. 1a).

The TTZ and TMZ were initially thought to be continuous and have formed as a result of the collision and subsequent indention of the Slave craton into the Rae craton, with the GSLsz acting as a dextral strike-slip structure (Hoffman, 1987). However, recent geochronologic and isotopic data have cast doubt on the contiguous nature of the TTZ and TMZ. Instead, the north and south sections of the Slave–Rae boundary may have formed at a similar time but in distinctly different tectonic environments (Chacko, De, Creaser, & Muehlenbachs, 2000; Card, Bethune, Davis, Rayner, & Ashton, 2014; Berman et al., 2018; Whalen, Berman, Davis, Sanborn-Barrie, & Nadeau, 2018). The TTZ is interpreted as a continental arc that is related to the closure of an oceanic basin between the Slave craton and the northwestern part of the Rae craton at ca. 1.97 Ga during the Thelon orogeny (Hoffman, 1987; Thériault, 1992; Whalen et al., 2018). In contrast, the TMZ is interpreted to have formed in a plate-interior rather than plate-margin setting (Chacko et al., 2000; Schultz et al., 2007). In this model, which is supported by the absence of a mantle signature in the chemistry of TMZ intrusions, the high-grade metamorphism and magmatism that characterizes the TMZ is the result of crustal thickening that itself was

caused by far-field stresses associated with an active plate boundary located either to the west of the adjacent Buffalo Head terrane or to the east of the Rae craton (Chacko et al., 2000).

The TTZ records slightly older magmatic ages (2.07–1.96 Ga; Berman et al., 2018) than the TMZ (1.99–1.92 Ga; Bostock & Loveridge, 1988; Bostock, Van Breemen, & Loveridge, 1987, 1991; Chacko et al., 2000). However, this trend is reversed for the metamorphic ages, with older metamorphic ages in the TMZ (1.94–1.92 Ga; McDonough, McNicoll, Schetselaar, & Grover, 2000; Bethune, Berman, Rayner, & Ashton, 2013) and younger metamorphic ages in the TTZ (1.92–1.89 Ga; Berman et al., 2018). Further complicating matters, in the Union Island Group (part of the Great Slave Supergroup), which is located along the southeast margin of the Slave craton and adjacent to the GSLsz (Fig. 2a), there is evidence for rift volcanism at ca. 2.05 Ga (Sheen et al., 2019). Based on these findings, Sheen et al. (2019) suggest that the Slave and Rae cratons may have formed a contiguous crustal block prior to ca. 2.05 Ga rifting.

The interpretation of Sheen et al. (2019) is consistent with models for the formation of Laurentia that include an earlier collision of Slave and Rae cratons during the ca. 2.5–2.3 Ga Arrowsmith orogeny, that is now recognized along much of the western margin of the Rae craton (McNicoll, Thériault, & McDonough, 2000; Hartlaub, Heaman, Chacko, & Ashton, 2007; Schultz et al., 2007; Tersmette, 2012; Berman et al., 2013). Evidence in support of the Arrowsmith orogeny includes bimodal magmatism at 2.50–2.45 Ga (Shultz et al., 2007; Tersmette, 2012), silicic magmatism at 2.49–2.47 Ga (Davis, Berman, & MacKinnon, 2013), and the intrusion of post-orogenic granites at ca. 2.3 Ga (Hartlaub et al., 2007; Tersmette, 2012). Metamorphism associated with the Arrowsmith orogeny range from upper-amphibolite to granulite facies between ca. 2.5–2.3 Ga, and together with the magmatism, likely represents

either an Andean-type margin with associated continental arc magmatism (Berman et al., 2013) or a Himalayan-style collision (Schultz et al., 2007; Tersmette, 2012).

With the available data, it is unclear how both the timing and tectonic setting of the GSLsz relate to the formation of the TTZ and TMZ. As the central segment of the Slave–Rae boundary, the GSLsz itself can be delineated over 1300 km using aeromagnetic data, from the foothills of the Rocky Mountains in the west to the Thelon Basin in the east (Fig. 1b). The mylonites of the GSLsz form a continuous structure that joins the north-trending linear magnetic highs of the TTZ and the TMZ (Fig. 1b). Kinematic indicators within the GSLsz record dextral strike-slip motion and, based on reconstructions using the aeromagnetic data, the GSLsz accommodated over 700 km of dextral displacement (Hoffman, 1988). Geochronological constraints from the GSLsz are sparse, and the existing data were not collected with modern methods so we are unable to assess whether they represent mixing of multiple age domains. The best estimates of the time of deformation, based on zircon U-Pb data from variably deformed granitic dykes, indicate that the GSLsz first became active sometime between ca. 2.00 and 1.86 Ga, possibly reactivating an earlier ca. 2.56 Ga structure (Bowring, Schmus, & Hoffman, 1984; Hanmer et al., 1992). The cessation of ductile shear in the GSLsz is indirectly constrained by an unconformably overlying quartzite of the Great Slave Supergroup, which yields a maximum deposition age of 1857 ± 11 Ma (Bowring et al., 1984).

Following the main ductile shearing event, the GSLsz and the adjacent southern margin of the Slave craton were dextrally offset by the McDonald fault (Bowring et al., 1984; Fig. 2). Both the McDonald fault and the brittle component of the conjugate sinistral Bathurst fault (Gibb, 1978; Fig. 1) are reported to have been active sometime after ca. 1.84 Ga (Henderson &

Loveridge, 1990; Ma, Kellett, Godin, & Jercinovic, 2019) and prior to deposition of the Thelon basin at ca. 1.72 Ga (Miller, Cumming, & Krstic, 1989; Fig. 1).

If the hypothesis that the TTZ and the TMZ do not define a continuous orogenic belt is correct, and/or the Slave and Rae cratons first collided during the Arrowsmith orogeny, then how does the GSLsz relate to the TTZ and TMZ in terms of both timing and tectonic affinity? In this paper, we provide new *P–T* estimates for representative samples from the GSLsz, which is the first step in elucidating the tectonometamorphic history of the central Slave–Rae boundary.

3   FIELD RELATIONS AND SAMPLE SELECTION

The width of individual map units within the GSLsz narrows with decreasing metamorphic grade (Hanmer et al., 1992), from ~20 km for the granulite, ~10 km for the upper-amphibolite mylonite, ~1 km for the epidote-amphibolite mylonite, and ~100 m for the greenschist ultramylonite. Two major brittle faults, with unknown offsets, run parallel to the strike of the mylonitic foliation (Fig. 2). To the north, the McDonald fault delimits the northernmost boundary of the GSLsz, juxtaposing greenschist ultramylonite against foliated plutonic rocks from the Slave craton and volcanic and sedimentary units from the Union Island Group. The second fault, which we term the Rocher River fault, runs through the centre of the GSLsz and separates epidote-amphibolite mylonite from greenschist ultramylonite. In addition to the metamorphic juxtaposition, the Rocher River fault divides the southwestern portion of the exposed GSLsz into two structural domains. South of the Rocher River fault, the mylonitic foliation strikes NE–SW, parallel to the strike of the fault. Whereas, to the north of the Rocher River fault, the mylonitic fabric strikes NNE–SSW and appears to be cut by the fault.

Recent glaciation and the present-day arid climate contribute to near-continuous bedrock exposure in the southwestern portion of the exposed GSLsz. With the exception of the

juxtaposition of units along late, minor brittle faults, the boundaries between the map units are diffuse and can be seen to be the result of lower metamorphic-grade assemblages superimposed on higher-grade rocks. For example, the boundary between the upper-amphibolite and epidote-amphibolite map unit occurs over ~100 m, with a progressive increase in the prevalance of the epidote-amphibolite assemblage overprint with distance into the area mapped as epidote-amphibolite facies. The overprinting of former, higher-grade metamorphic assemblages by lower-grade assemblages is associated with the strain related to pervasive right-lateral shear. Field evidence for the progressive nature of this overprint and its association with ductile deformation include the observation of upper-amphibolite mineral assemblages (garnet-present) preserved in the low-strain cores of mafic boudins that are flanked by garnet-absent and epidote-bearing high-strain margins (Fig. S1). Given the progressive nature of the map-unit boundaries, we adopt the convention used by previous workers and mark the boundaries for each unit based on the first appearance of the lower-grade mineral assemblage.

In total, 60 samples and 50 cores were collected along two profiles that transect the southwestern exposure of the GSLsz (Fig. 2c) with an additional eight samples and five cores collected along strike (~90 km to the northeast) from an area previously mapped as granulite facies metaplutonic and metasedimentary units (Fig. 2b). Of all samples collected, six representative samples were selected to provide quantitative P–T estimates for the granulite, upper-amphibolite mylonite, epidote-amphibolite mylonite and greenschist ultramylonite map units.

4 METHODS

4.1 Analytical Methods

For the purpose of petrological modelling, effective bulk compositions were determined by combining mineral composition data with thin-section X-ray phase maps. Thin-section X-ray phase maps and mineral-area analyses were obtained at SGS, Burnaby, Canada using the QEMSCAN energy dispersive spectrum-based (EDS) automated mineralogy system mounted on a tungsten-source Tescan Vega scanning electron microscope. Entire thin sections were analysed at an excitation voltage of 20 kV and beam current of 10 nA, with a step size of 7 μm, providing high-resolution modal (area) analyses for all phases (Table 1). The fully automated QEMSCAN system integrates backscattered electron (BSE) and EDS signals to characterize polished sample surfaces (Gottlieb et al., 2000). Maps of BSE brightness were calibrated against quartz, gold, and copper standards. Spectra were processed using user-defined species identification protocol files that characterize phases on the basis of characteristic EDS spectra and BSE intensity. The high-resolution phase maps for all samples described in this study are available in the supplementary information file (Fig. S2).

Mineral compositions were obtained at the University of British Columbia using a CAMECA SX-50 electron microprobe analyser (EMPA). Operating conditions include an excitation voltage of 15 kV, a beam current of 20 nA, a peak count time of 20 s with a background count time of 10 s, and a spot size of 5 μm. The standards, X-ray lines and crystals used are provided in Appendix S1. Data reduction was performed using the method of Pouchou and Pichoir (1985). For all phases, locations for analysis were chosen to represent the full range of petrographic positions (e.g., matrix, corona, porphyroblast core and rim), and multiple spots were collected from select grains to assess inter- and intra-crystalline compositional variation. For all applicable phases, Fe^{3+} was calculated on the basis of charge-balance using the software AX 6.2 (Holland, 2018).

4.2 Petrological modelling approach

All phase diagrams were calculated using the petrological modelling software Theriak–Domino (de Capitani & Petrakakis, 2010). Two different sets of activity–composition models and thermodynamic datasets were used in this study, the choice of which depended on sample composition. For the pelitic and metagranodioritic samples (GSL-18-BD7, GSL-18-BD25, GSL-18-C47, and GSL-18-C53) modelling was undertaken in the $MnO–Na_2O–CaO–K_2O–FeO–MgO–Al_2O_3–SiO_2–H_2O–TiO_2–O_2$ (MnNCKFMASHTO) chemical system using the internally consistent thermodynamic dataset ds-55 of Holland and Powell (1998) (updated to August 2004) and activity–composition relations for melt, biotite and ilmenite (White, Powell, & Holland, 2007), feldspar (Holland & Powell, 2003), white mica (Coggon & Holland, 2002), and garnet (White et al., 2007). Modelling of mafic samples (GSL-18-BD26 and GSL-18-C50) was undertaken in the $Na_2O–CaO–K_2O–FeO–MgO–Al_2O_3–SiO_2–H_2O–TiO_2–O_2$ (NCKFMASHTO) chemical system using the internally consistent thermodynamic dataset ds-62 of Holland and Powell (2011) (updated to February 2012) with activity–composition models for melt, augite, and hornblende (Green et al., 2016); garnet, orthopyroxene, biotite, and chlorite (White, Powell, Holland, Johnson, & Green, 2014); olivine and epidote (Holland & Powell, 2011); magnetite–spinel (White, Powell, & Clarke, 2002); ilmenite–hematite (White, Powell, Holland, & Worley, 2000); C1 plagioclase and K-feldspar (Holland & Powell, 2003).

While both thermodynamic datasets were tested for all samples, ds-55 was chosen for the pelitic and metagranodioritic rocks over the more recent ds-62 because it better predicted the observed mineral assemblages, and in particular, the composition and stability of garnet in these samples (c.f., Starr, Pattison, & Ames, 2019; Waters, 2019). Dataset ds-62, with the associated activity–composition models, replicated the observed mineral assemblages for the mafic samples reasonably well with the one exception of augite, which was predicted to be stable over a wide-

range of conditions but is not present in either sample. The overstabilization of 1–2 modal %

augite in petrological models at amphibolite facies conditions has been documented by multiple

recent studies (Forshaw, Waters, Pattison, Palin, & Gopon, 2019; Weller, Copley, Miller, Palin,

& Dyck, 2019). As such, we did not rely upon the occurrence of augite in the calculated

pseudosections for mafic samples for our interpretation of P–T conditions.

Uncertainty on the absolute positions of phase assemblage boundaries in pressure–

temperature space generally do not exceed ±20–30 °C and ± 0.05 GPa at 1 S.D. (Powell &

Holland, 2008; Palin, Weller, Waters, & Dyck, 2016), although the relative errors may be

smaller when comparing results generated using the same dataset and associated activity–

composition models. Since the results we present here were calculated using two datasets, the

absolute errors remain an important consideration when we compare the P–T estimates among

samples.

The amount of H_2O was set to minimally saturate (i.e., 0.05 mol% free H_2O) the

assemblage in the immediate sub-solidus at a pressure of 0.7 GPa for all samples with peak

mineral assemblages formed above the solidus (see Fig. S3 in supplementary material for an

example T–X_{H2O} diagram). Bulk rock $X_{Fe}^{3+} = Fe^{3+}/(Fe_{total})$ was set for each sample and is a

function of the Fe^{3+} determined for all ferric minerals by stoichiometric charge-balance (Table 2).

The effective bulk compositions for all phase diagrams discussed below are provided in Table 3.

4.3 Thermobarometry

To complement the petrological modelling and provide independent constraints on the

metamorphic conditions recorded in our samples, we applied two sets of independent

thermometers, the Ti-in-biotite thermometer of (Henry, Guidotti, & Thomson, 2005) and the

amphibole–plagioclase thermometers of (Holland & Blundy, 1994). Precision of the Ti-in-

biotite thermometer varies with temperature, with the largest 1σ uncertainty reported as ± 24 ºC for greenschist facies conditions, decreasing to ± 12 ºC for amphibolite and granulite facies (Henry et al., 2005). For consistency, we report all Ti-in-biotite temperatures with the larger ± 24 ºC uncertainty. Since all of the rocks we studied are quartz-bearing, we applied both the edenite–tremolite and edenite–richterite thermometers, which both have a 1 σ uncertainty of ± 40 ºC (Holland & Blundy, 1994). The application of the edenite–richterite thermometer was restricted to samples with X_{Ab} < 90 because the equilibrium constant for this reaction requires an accurate estimate of the activity of anorthite.

In addition to these independent thermometers, for all samples with suitable mineral assemblages, we used the average *PT* (avPT) and average *T* (avT) functions in THERMOCALC (versions tc340i with ds-62 and tc333 with ds-55), which performs a least-squares regression on a set of independent end-member reactions (Powell & Holland, 1994). For consistency with the petrological modelling, end-member activities for mafic samples were calculated using AX 6.2 (Holland, 2018) and using AX (Holland & Powell, 2009) for pelitic and metagranodioritic samples. The 1 σ uncertainty for average *PT* calculations is expressed as an error ellipse, the dimension of which scales with the collective fit of the end-member reactions (Powell & Holland, 1994).

5   PETROGRAPHY & MINERAL CHEMISTRY

5.1.1   GSL-18-C47, Granulite facies paragneiss

Sample GSL-18-C47 was collected from a metre-scale pelitic paragneiss raft within a larger body of garnet-monzogranite (Fig. 2b). The thin-section from this sample comprises garnet (~8%), sillimanite (~11%), biotite (~12%), quartz (~26%), plagioclase (~28%), and K-feldspar

(~9%) with minor muscovite and accessory titanite and ilmenite. Centimetre-scale blades of apparent kyanite were observed in field and hand-sample. However, evaluation of the thin-section reveals that sillimanite has fully replaced kyanite (Fig. 3a). The sample has no clear foliation or lineation, although a record of high-temperature ductile deformation is preserved as chessboard subgrains in quartz (Fig. 3b). Garnet occurs as porphyroblasts 1–2 mm in diameter, and EMPA line-profiles across garnet reveal a flat profile, with a composition of $Alm_{0.70}Prp_{0.21}Sps_{0.02}Grs_{0.04}And_{0.02}$ (Fig. 4a; Table 2), for which Alm = almandine = $Fe^{2+}/(Fe^{2+} + Fe^{3+} + Mg + Ca + Mn)$, Prp = pryrope = $Mg/(Fe^{2+} + Fe^{3+} + Mg + Ca + Mn)$, Sps = spessartine = $Mn/(Fe^{2+} + Fe^{3+} + Mg + Ca + Mn)$, Grs = grossular = $Ca/(Fe^{2+} + Fe^{3+} + Mg + Ca + Mn)$, and And = andradite = $Fe^{3+}/(Fe^{2+} + Fe^{3+} + Mg + Ca + Mn)$. While there is no significant compositional zoning in garnet, there is a slight increase of Mn and Fe content in the outermost rim. Biotite occurs both in centimetre-sized schlieren (intergrown with prismatic sillimanite) and along garnet grain boundaries. Based on a 22-oxygen calculation, biotite contains Ti = 0.43–0.44 apfu (atoms per formula unit) and has a XMg = $Mg/(Mg + Fe^{2+})$ = 0.44 (Table 2). Plagioclase and K-feldspar are present as subhedral matrix grains with an average XAb = $Na/(Ca + Na + K)$ 0.60 and 0.13, respectively (Table 2). A minor amount (<1%) of muscovite is intergrown with fine-grained biotite, quartz and sillimanite, and is likely of retrograde origin.

5.1.2   GSL-18-BD25, Upper-amphibolite facies mylonitic schist

Sample GSL-18-BD25 is a pelitic and migmatitic schist (Fig. 2c; Fig. 3c). The thin-section from this sample comprises garnet (~2%), fibrolitic sillimanite (~1%), biotite (~14%), chlorite (~2%), quartz (~36%), plagioclase (~37%), and K-feldspar (~12%) with accessory rutile and ilmenite (Table 2). Alignment of biotite, fibrolitic sillimanite, quartz ribbons, and boudinaged K-feldspar define a penetrative foliation (Fig. 3c) and oblique shear-band fabric. Quartz ribbons exhibit a

crystallographic preferred orientation under the gypsum plate. The outcrop from which this sample and GSL-18-BD26 were collected has decametre-scale intercalations of mafic and pelitic rocks, with a distinct leucosome and melanosome developed in both lithologies (Fig. 3d). On the thin-section scale, leucosomes comprise recrystallized quartz, K-feldspar and highly sericitized plagioclase (white-mica alteration). Melanosomes comprise biotite, sillimanite and retrograde chlorite (Fig. 3c). Garnet occurs in the more aluminous melanosomes as porphyroclasts up to ~4 mm in diameter that are partially replaced by biotite along their margins. Analyses of garnet reveal a lack of internal zoning, with the exception of an increase of Mn and Fe in the outermost resorbed rim (Fig. 4b). We interpret the core composition of $Alm_{0.73}Prp_{0.18}Sps_{0.02}Grs_{0.05}And_{0.02}$ to reflect the final stage of diffusional equilibration between garnet and the matrix minerals. There is no significant difference in composition between the matrix biotite and biotite grains adjacent to garnet rims, with Ti = 0.41 apfu and X_{Mg} = 0.44, based on a 22-oxygen formula unit (Table 2). There are no detectable differences in the major element compositions of plagioclase or K-feldspar, independent of grain/porphyroclast morphology. Plagioclase has a mean X_{Ab} = 0.71 and K-feldspar has a X_{Ab} = 0.14 (Table 2).

5.1.3 GSL-18-BD26, Upper-amphibolite facies garnet amphibolite

Collected from the same outcrop as the previous sample (Fig 2c), GSL-18-BD26 is a metabasaltic garnet amphibolite. The thin-section for this sample contains garnet (~4%), amphibole (~56%), quartz (~10%), plagioclase (~19%), with accessory ilmenite, titanite and apatite. The matrix exhibits a fine-grained granoblastic texture with a moderately well-developed foliation defined by elongate quartz grains (Fig. 3e). In garnet, fine-grained inclusion trails of quartz and ilmenite exhibit a slightly sigmoidal shape (Fig. 3e), which indicates syn-deformation garnet growth. Garnet exhibits no compositional zoning, with a uniform

$Alm_{0.60}Prp_{0.13}Sps_{0.04}Grs_{0.21}And_{0.02}$ composition across EMPA line-profiles (Fig. 4c). Based on the classification scheme of Leake et al., (1997, 2004), the amphibole is Tschermakite, with Si = 6.28–6.53 apfu (per 23 oxygens), Na + K (A-site) = 0.25–0.40 apfu, Na (B-site) = 0.12–0.17 apfu, and XMg = 0.49–0.56 (Fig. 5., Table 2). Leucosome comprising quartz, plagioclase, and minor K-feldspar is present as millimetre-to-centimetre sized, foliation-parallel segregates (Fig. 3f). The composition of plagioclase and K-feldspar is uniform amongst both leucosome and matrix grains, with an average plagioclase XAb = 0.49 and K-feldspar XAb = 0.02 (Table 2).

5.1.4   GSL-18-C53, Epidote-amphibolite facies mylonitic schist

Sample GSL-18-C53 is a strongly deformed garnet–biotite–chlorite mylonitic schist collected from a metre-wide pelitic layer at the same outcrop as GSL-18-C50 (Fig. 2c). The thin-section for GSL-18-C53 contains garnet (~11%), prismatic sillimanite (~0.5%), biotite (~14%), chlorite (~8%), muscovite (~14), quartz (~24%), plagioclase (~23%), and K-feldspar (~4%) with accessory titanite, apatite, and ilmenite. In outcrop, garnet occurs as centimetre-sized winged porphyroclasts (Fig. S2) with foliation parallel quartzofeldspathic strain shadows (Fig. 6a). The penetrative foliation and dextral shear-band fabric is defined by the alignment of chlorite, biotite, and quartz ribbons (Fig. 6a). EMPA line-profiles across garnet reveal a distinct core-to-rim zoning, with a high-grossular and low-pyrope core, $Alm_{0.66}Prp_{0.07}Sps_{0.06}Grs_{0.19}And_{0.06}$, and low-grossular and high-pyrope rim, $Alm_{0.74}Prp_{0.17}Sps_{0.02}Grs_{0.05}And_{0.02}$ (Fig. 4d, Table 2). The 'bell-shaped' grossular and spessartine profile is interpreted as prograde growth, with a local depletion in manganese during initial stages of growth (Kohn & Spear, 2000). Chlorite and biotite embay the outermost rim of garnet, and chlorite fills through-going fractures that were avoided when setting EMPA points (Fig. 4e). An increase of Mn-content in the outermost 50 μm rim of garnet is interpreted as Mn-uptake during garnet resorption (Fig. 4d). Millimetre-sized porphyroclasts

of plagioclase and K-feldspar are rounded and wrapped by a very fine-grained matrix of biotite, chlorite and quartz (Fig. 4e). Light-brown biotite occurs as both a very fine-grained matrix phase and intergrown with prismatic sillimanite in millimetre-sized schlieren (Fig. 6b). There is no significant difference in biotite composition between the two petrographic positions, with Ti = 0.39 apfu and XMg = 0.40 based on a 22-oxygen formula unit (Table 2). Chlorite has XMg = 0.38 and XFe^{3+} = Fe^{3+}/(Fe^{2+} + Fe^{3+}) = 0.11. Plagioclase is heavily sericitized, to the extent of complete replacement by radial muscovite in some grains (Fig. 6c). Rare, unaltered plagioclase grains have a mean XAb = 0.59, and XAb = 0.11 in K-feldspar.

5.1.5   GSL-18-C50, Epidote-amphibolite facies mylonitic amphibolite

Sample GSL-18-C50 was collected from a 2-metre-wide mafic layer at the same outcrop as GSL-18-C53 (Fig. 2c). Similar to the previous sample, there are centimetre-sized, winged porphyroclasts surrounded by a very fine-grained mylonitic matrix (Fig. 6d). There is, however, no garnet present in the thin-section, which is made up of clinozoisite (~21%), amphibole (~12%), biotite (~3%), titanite (~3%), chlorite (~6%), quartz (~27%), albite (~10%), and K-feldspar (~13%) with accessory apatite. Clinozoisite, amphibole, and titanite completely replace what are presumed to be former garnet porphyroclasts, which are rimmed by fine-grained biotite and surrounded by a matrix of chlorite, plagioclase, quartz, and K-feldspar (Fig. 6e). Clinozoisite, which also fills cross-cutting veins, has a uniform composition across the sample with Fe^{3+} = 0.72–0.74 apfu and Si = 3.09–3.13 based on a 12.5-oxygen formula unit (Table 2). Amphibole is present within the pseudomorphed porphyroclast and as an array of grains that follows the shape of the winged strain markers (Fig. 6e). Based on the classification scheme of Leake et al. (1997, 2004), the amphibole is ferropargasite/hastingite, with Si = 6.15–6.35 apfu (per 23 oxygens), Na + K (A-site) = 0.61–0.70 apfu, Na (B-site) = 0.03–0.05 apfu, and X_{Mg} =

0.25–0.30 (Fig. 5; Table 2). Rhombic grains of titanite up to 1 mm in length are abundant in the pseudomorph and exhibit a shape preferred orientation oblique to matrix foliation (Fig. 6e). Matrix biotite is light-brown coloured and appears to be partially replaced by chlorite. Due to the fine grain size of biotite, its composition could not be measured accurately. The coarser clots of matrix chlorite have $X_{Mg} = 0.31$ and $X_{Fe^{3+}} = 0.10$. Feldspar porphyroclasts present evidence of white mica alteration, with the least altered domains of albite yielding an average $X_{Ab} = 0.97$ and average K-feldspar $X_{Ab} = 0.08$.

5.1.6   GSL-18-BD7, Greenschist facies ultramylonite

Sample GSL-18-BD7 is a fine-grained granodioritic ultramylonite (Fig. 2c). This sample is made up of amphibole (~25%), epidote (~1%), titanite (1–2%), chlorite (~4%), biotite (~2%), muscovite (~7%), plagioclase (~43%), quartz (~12%) and K-feldspar (~5%), with accessory apatite. This sample exhibits millimetre-scale compositional layering with varying proportions of amphibole, chlorite, quartz and plagioclase in each layer (Fig. 6f). Amphibole is present in the matrix, in cross-cutting veins and as medium-grained clots. Despite having a range of Si values from 6.57 to 7.34 apfu (per 23 oxygens), all amphibole is magnesiohornblende, with Na + K (A-site) = 0.10–0.38 apfu, Na (B-site) = 0.01–0.08 apfu, and XMg = 0.58–0.73 (Fig. 5; Table 2). Plagioclase is present as fine-grained porphyroclasts with an average XAb = 0.71 (Table 2). In the matrix surrounding these porphyroclasts, the most abundant feldspar phase is highly sericitized albite. K-feldspar occurs as very-fine grained aggregates that are associated with the more amphibole-rich layers. The average XAb of K-feldspar is 0.04 (Table 2). Epidote is found throughout the matrix with a Fe^{3+} = 0.74–0.79 apfu and Si = 2.73–2.97 apfu on the basis of 12.5 oxygen (Table 2). Chlorite has an average XMg = 0.46 and XFe^{3+} = 0.12. Light-brown biotite is found as a minor phase forming epitactic intergrowths with chlorite. Given the very fine-grained

nature of biotite-chlorite intergrowths, we were unable to accurately measure biotite composition.

6   PETROLOGICAL MODELLING & THERMOBAROMETRY

The principle aim of petrological analyses is to determine the pressure and temperature conditions at which the GSLsz rocks underwent their final stage of ductile deformation and metamorphic recrystallization. However, as is commonly the case with garnet-bearing metamorphic rocks, portions of the prograde and/or retrograde metamorphic histories are also preserved (Spear & Selverstone, 1983; St-Onge, 1987). Here, we combine phase diagram-based petrological modelling with conventional multi-equilibria and single-phase thermobarometry to determine the metamorphic histories of the GSLsz rocks.

6.1 Pressure–temperature estimates

6.1.1   GSL-18-C47 – Granulite facies paragneiss

Figure 7 presents calculated equilibria for GSL-18-C47. The diagram is contoured with isomodes of kyanite and garnet compositional isopleths (pyrope and grossular). As a consequence of setting H_2O to minimally saturate the solidus, melt constitutes a minor phase (<1 modal %) in the immediate supra-solidus field. Only at temperatures above the vapour-absent muscovite dehydration reaction does any significant melting occur, which is accompanied by the growth of an aluminosilicate phase (Dyck, Waters, St-Onge, & Searle, 2019). We interpret the aluminosilicate microstructures to have formed along a prograde path that started in the kyanite stability field with 3–4 modal % growth during muscovite melting. The flat compositional profiles in garnets from this sample (Fig 4a) indicate that garnet fully equilibrated with the matrix phases at some point in the rock's history. By comparing the measured garnet chemistry against the calculated isopleths of pyrope and grossular we estimate that the final equilibration of

garnet occurred at ~0.85 GPa and ~785 ºC. At these conditions, some biotite still remains in the predicted assemblage, and although the assemblage is not fully dehydrated, it straddles the boundary between upper-amphibolite and granulite. With a two-pyroxene assemblage reported from nearby mafic lithologies (Hanmer, 1988) and confirmed in our own sample collection, we follow previous workers in mapping this unit as granulite facies. The intergrowth of muscovite and sillimanite indicates that the rock underwent both decompression and cooling following peak metamorphism, remaining in the sillimanite stability field during retrograde re-equilibration. When combined with the Ti-in-biotite results, we interpret that this final stage of deformation and (local) equilibration took place at ~0.7 GPa and ~710 ºC.

We ran two sets of avPT calculations, one with the garnet core composition and a second using the outermost garnet rim composition. Uncertainty ellipses for results of both calculations are presented in Fig. 7. Both avPT results are within error of temperature estimates given by Ti-in-biotite. However, we are cautious in interpreting either of the avPT results as being geologically meaningful due to the difficulty in assessing the extent to which matrix biotite and plagioclase re-equilibrated during garnet resorption.

6.1.2 GSL-18-BD25 – Upper-amphibolite facies mylonitic schist

Fig. 8a presents a pseudosection for GSL-18-BD25 calculated at 0.5–1.3 GPa and 600–900 ºC. Garnet is only stable at the higher end of the *P–T* conditions considered. As with the previous sample, we interpret the homogeneous compositional profile in garnet (Fig 4b) to reflect the final stage of diffusional equilibration between garnet and the matrix minerals, at ~1.1 GPa and ~760 ºC. At these conditions, garnet would have reached equilibrium with a matrix assemblage of melt–biotite–K-feldspar–plagioclase–kyanite. As sillimanite is the only aluminosilicate phase found in the matrix and the temperatures under which both garnet and sillimanite are stable are

higher than those indicated by the pyrope and grossular isopleths, we interpret garnet as a porphyroclastic metastable phase. This interpretation is based on the simple assumption that once temperatures were high enough for garnet to effectively maintain equilibrium with matrix phases, the garnet composition would continue to re-equilibrate with increasing temperatures. If this were the case, and the rock had reached a temperature at which garnet was in equilibrium with sillimanite, we would expect to see a garnet composition that was 20–30% more Mg-rich.

Our best estimate for the conditions at which the mylonitic fabric was developed is given by the overlap of the Ti-in-biotite results with the stability field for the observed peak metamorphic assemblage of melt–biotite–K-feldspar–plagioclase–sillimanite at ~0.7 GPa and ~710 ºC. The avPT results superficially appear to broadly overlap the conditions that we interpret as the final stage of equilibrium. However, there is poor agreement between the modelled isopleths and the avPT results generated with garnet core composition. If the garnet rim composition is used for the avPT calculation, the results are considerably less precise (Fig. 8a).

6.1.3 GSL-18-BD26 – Upper-amphibolite facies garnet amphibolite

Fig. 8b presents a pseudosection for GSL-18-BD26 calculated at *P–T* conditions of 0.5–1.0 GPa and 500–900 ºC. Accounting for the overstabilization of augite, the observed mineral assemblage of amphibole–garnet–plagioclase–quartz (+melt) is found to be stable over a wide range of upper-amphibolite facies conditions. To further constrain the conditions of peak metamorphism, we plotted the observed garnet and amphibole chemistry on the modelled pyrope, grossular, and Si-in-amphibole isopleths (Fig. 8b). The pseudosection approach yields peak-metamorphic conditions for GSL-18-BD26 at ~0.9 GPa and ~800 ºC. There is considerable overlap in the temperatures predicted by amphibole-plagioclase thermometers and those from the pseudosection results. Furthermore, the avPT results are within error of the results generated by

the other methods, albeit shifted towards lower temperatures (Fig 8b). In these calculations, the fluid was considered to be pure H_2O. Decreasing the activity of H_2O would reduce the P–T estimates by ~0.01 GPa and ~10 ºC per 0.1 increment of $X(H_2O)$.

6.1.4   GSL-18-C53 – Epidote-amphibolite facies mylonitic schist

In rocks for which the equilibrium volume (and the corresponding effective bulk composition) changed alongside the evolution of P–T conditions (i.e., with the chemical isolation of garnet cores), segments of prograde and/or retrograde history may also be preserved (Spear & Selverstone, 1983). In such cases, fractionation (modification) of the effective bulk composition may provide a more accurate estimate of the equilibration conditions (e.g., Evans, 2004; Tinkham & Ghent, 2005; Konrad-Schmolke, O'Brien, de Capitani, & Carswell, 2008). The subsolidus region of the phase diagram constructed for GSL-18-C53 in Fig. 9a was generated using the integrated composition and modal proportions of all phases, including the garnet core domain with water considered in excess. A second, fractionated, minimally water-saturated, phase diagram that excludes the garnet core domain was generated to constrain the conditions under which the rim of the garnet grew. For simplicity, we merge the two pseudosections along the water-saturated solidus (Fig. 9a).

Pyrope and grossular isopleths constrain garnet core growth to ~0.75 GPa and ~550 ºC, with a matrix assemblage of muscovite–biotite–epidote–plagioclase–kyanite–quartz–ilmenite. The measured garnet rim composition is not replicated anywhere within the unfractionated P–T region of interest. Instead, the pyrope and grossular isopleths generated with the fractionated effective bulk composition constrain the conditions of garnet rim growth to ~0.8 GPa and ~725 ºC, in equilibrium with the observed peak metamorphic assemblage of biotite–plagioclase–quartz–sillimanite–quartz–ilmenite (+melt).

AvPT results for GSL-18-C53, using garnet rim compositions, plot below the considered *P–T* range with a least square mean of 0.3 ± 0.1 GPa and 488 ± 13 ºC (correlation coefficient = 0.265 and significance of fit = 0.08). The presence of retrograde chlorite in the matrix shear bands and absence of retrograde staurolite is an indication that, despite continued deformation, equilibrium (on the thin-section scale) was not maintained as the rock cooled. As such, we do not interpret the avPT results as being geologically meaningful. Instead the retrograde history is loosely constrained by the Ti-in-biotite temperatures and the upper-temperature stability of chlorite. Biotite last equilibrated at 686 ± 24 ºC in the sillimanite stability field. The alignment of chlorite within the shear fabric indicates the rock continued to deform as the rock cooled below ~600 ºC, at unknown pressures.

6.1.5   GSL-18-C50 – Epidote-amphibolite facies mylonitic amphibolite

We generated two pseudosections, presented in combination in Fig. 9b, at *P–T* conditions of 0.5–1.1 GPa and 400–800 ºC for sample GSL-18-C50 because it exhibits petrological evidence for significant hydration following peak metamorphism. One set of equilibria relations was calculated with H_2O as an excess phase and was used for evaluating subsolidus phase stability (blue field shading). We used a second pseudosection (red field shading), constructed with H_2O set to minimally saturated at the 0.7 GPa solidus, to evaluate the stability of garnet in melt-bearing assemblages. The results from both calculations were merged along the H_2O-present solidus and are shown in Fig. 9b.

If we consider the close proximity of this sample to GSL-18-C53, and assume similar peak metamorphic conditions for both samples, then the peak assemblage of GSL-18-C50 would have garnet in equilibrium with amphibole–plagioclase–K-feldspar–quartz–ilmenite–titanite (+melt). While there is no garnet remaining in this sample, we interpret the rounded shape and

size of the porphyroclastic microstructure (Fig. 6e) as an indication that garnet was once stable and persisted during the initial development of mylonitic fabric. The results from the edenite–tremolite thermometer further indicate that this rock experienced temperatures in excess of ~650 ºC. However, the amphibole and plagioclase compositions may have equilibrated during retrograde metamorphism and deformation.

It was not possible to determine the extent to which this rock underwent decompression prior to the growth of the retrograde assemblage because the observed assemblage of amphibole–albite–clinozoisite–biotite–titanite–quartz–rutile is stable over a broad pressure range (0.4–1.0 GPa). Similarly, without garnet there is an insufficient number of independent pressure-sensitive end-member reactions to calculate an avPT result. Instead, we made an avT calculation (excluding sanidine and anorthite), which yields a mean temperature estimate of 503 ± 16 ºC (significance of fit = 1.21) for reactions between amphibole–albite–clinozoisite–chlorite–ilmenite–quartz–H_2O.

6.1.6   GSL-18-BD7 – Greenschist facies ultramylonite

Fig. 10 presents phase equilibria for sample GSL-18-BD7 at *P–T* conditions of 0.2–0.7 GPa and 400–650 ºC. The overlapping stability of chlorite–epidote–K-feldspar ± biotite, all found in the finely recrystallized matrix of GSL-18-BD7, constrain the final temperature of deformation to ~415–445 ºC. This temperature estimate is independently corroborated by an avPT calculation, based on equilibrium between chlorite–plagioclase–amphibole–epidote–quartz–H_2O, which yields 0.4 ± 0.19 GPa and 442 ± 65 ºC (correlation coefficient = 0.986 and significance of fit = 1.13). When we combine the results from phase equilibria and avPT calculations, our best estimate for the conditions of greenschist-facies metamorphism in the GSLsz is ~0.4 GPa and ~430 ºC.

7 DISCUSSION & CONCLUSIONS

7.1 *P–T* synthesis and implications for Slave–Rae tectonics

Figure 11a summarizes the *P–T* results presented in this paper, overlain on a range of crustal thermal gradients typical of regional metamorphism (England & Thompson, 1984; Brown, 2007). Segments of clockwise *P–T* loops are recorded in samples from the granulite (GSL-18-C47), upper-amphibolite (GSL-18-BD25), and epidote amphibolite (GSL-18-53) units. Although there is a considerable range of final conditions of equilibrium for individual map units, spanning temperatures of ~430–800 ºC, the granulite, upper-amphibolite and epidote amphibolite samples all experienced peak metamorphism at similar *P–T* conditions (~0.85 GPa and ~750 ºC). The prograde record that is preserved in garnet chemistry and aluminosilicate microstructure indicates that metamorphism of the GSLsz rocks initially progressed under a thermal gradient of ~650 ºC·GPa^{-1} (assuming mean overburden density of 2750 kg·m^{-3}). In four of the six samples that we studied, there is a record of decompression and retrograde mineral growth associated with the development of a penetrative shear fabric. The *P–T* conditions of the final stage of equilibrium recorded by matrix minerals in all six samples collectively define a metamorphic field gradient of ~1000 ºC·GPa^{-1}.

The nested nature of the clockwise prograde *P–T* paths preserved in the GSLsz rocks is consistent with a single metamorphic event involving crustal thickening and Barrovian-style metamorphism (England & Thompson, 1984; Weller et al., 2013). The absolute timing of crustal thickening and the attendant development of metamorphic fabrics remains poorly constrained. However, in samples that we studied, it appears that crustal thickening either preceded or was coeval with ductile shear. This interpretation is, in part, supported by the absence of sigmoidal inclusion trails in garnet, which is consistent with crustal thickening preceding the development

of a penetrative shear fabric. The one exception we note is the slightly sigmoidal garnet inclusion trails found in sample GSL-18-BD26 (garnet amphibolite). However, this sample only exhibits a weak and non-penetrative shear fabric and so it likely remained unaffected by the dextral shear. Moreover, at the regional scale, it is unlikely that the lower-crustal metamorphic and deformation features of the GSLsz would have been isostatically uplifted and exhumed to be present at the current surface erosion level without an earlier stage of crustal thickening.

Given the present configuration of the Slave and Rae cratons, the most apparent cause of the crustal thickening is convergence between Slave and Rae. However, without reasonable constraints on the timing of the prograde metamorphism and the provenance of sedimentary material it is premature to speculate on the pre-GSLsz configuration of Slave and Rae. Moreover, the timing of the postulated transition from crustal thickening to lateral shear on the Slave–Rae margin is poorly documented. However, the elevated metamorphic field gradient and superposition of GSLsz fabrics on peak metamorphic assemblages implies that the ductile deformation associated with the GSLsz was active whilst the overthickened northern Rae margin was still relatively hot.

7.2 Metamorphic evolution of continental-scale shear systems

In the Sibson-Scholz model of fault zone structure, illustrated schematically in Fig. 11b, one or more zones of dominantly frictional deformation in the upper crust transition into zones of dominantly viscous deformation in the middle and lower crust, with the thickness of the deformed zones generally increasing with depth (Sibson, 1983; Scholz, 1988). Activity of a fault zone during exhumation by erosional unroofing commonly results in an overprinting sequence of down-temperature fault rocks (Sibson, 1977; Hanmer, 1988; Jefferies et al., 2006; Phillips & Searle, 2007; Norris & Toy, 2014). If deformation occurs over time scales shorter than required

for conductive relaxation of elevated crustal thermal gradients (< 10 Ma for continental collision (England & Thompson, 1984), < 100 Ma for margins with continental arcs (Xiao et al., 2005)) then the conditions of final equilibrium in all levels should reflect a similar geothermal gradient.

Shear heating associated with ductile deformation in the GSLsz is an additional process that might have impacted the recorded temperatures. The magnitude of that contribution to the heat budget is difficult to assess because of the simultaneous exhumation that accompanied deformation, which resulted in cooling at an unknown rate. Previous estimates of shear heating in major ductile shear zones without exhumation suggest shearing may elevate temperatures by 10s (e.g., Thacher and England, 1998) to 100s (e.g., Nabelek et al., 2010) of degrees. However, models that estimate significant shear heating (e.g., Nabelek et al., 2010) require stresses during ductile deformation that are considerably higher than those estimated by paleopiezometric analyses of similar shear zones (e.g., Platt & Behr, 2014; Chatzaras et al., 2015).

The improved *P–T* constraints provided by the present study are a significant development in discriminating between the GSLsz developing as a single structure active during one progressive deformation event, or a structure that was reactivated at different crustal levels during temporally distinct deformation events. The conditions of final equilibration, which fall on a single metamorphic field gradient despite spanning greenschist- to granulite-facies conditions (Fig. 11a), are consistent with all the mylonitic units having formed during a single portion of the orogenic cycle, within a sufficiently short duration of time that there would have been little change to the crust thermal gradient. Furthermore, the retrograde path of granulite facies sample GSL-18-C47 indicates that individual rock packages did indeed follow this apparent geothermal gradient during exhumation and cooling from a maximum burial depth of ~30 km (Fig. 11a).

7.3 Quantifying *P–T* in shear zones

The application of equilibrium thermodynamics to rocks that have experienced a protracted history of shear and dynamic recrystallization poses some significant challenges that warrant further discussion. While a range of thermobarometry and petrological modelling tools can be employed to quantify portions of the *P–T* history for a rock, correctly interpreting the *P–T* results requires knowing how equilibration volume evolves with both metamorphic grade and degree of strain (Marsh, Johnson, Yates, & West, 2009). One of the main challenges we faced in this study was determining mineral assemblages that chemically equilibrated together during the final stage of deformation and recrystallization. This is particularly important in samples with porphyroclasts because: 1) the partitioning of strain may trigger recrystallization and equilibration in the matrix phases but not the porphyroclastic phase (Koons, Rubie, & Fruch-Green, 1987), and 2) the length-scale of intracrystalline diffusion are greater in the porphyroclasts than the finer-grained matrix, which may result in porphyroclast cores that do not equilibrate with the matrix (Florence & Spear, 1995).

In shear zones, in which deforming matrix phases can more efficiently maintain chemical equilibrium (Koons et al., 1987), the application of thermobarometric equations that include garnet endmembers, whether it be by avPT, TWQ (Berman, 1991), or another program, should be used with caution on samples that show no evidence for retrograde equilibration. For example, the presence of locally manganese-rich garnet rims likely indicated rim resorption processes and intragranular transport (Tracy, 1982) and should be avoided. This point is well-illustrated in the samples that we studied, for which the disparity between the *P–T* results calculated by conventional thermobarometers and pseudosection modelling reflects disequilibrium between porphyroclastic garnet and matrix phases. We base this interpretation on the garnet compositional profiles for GSL-18-BD47, GSL-18-BD25, GSL-18-C53, all of which

reveal an enrichment of manganese in the outermost garnet rims. In these cases, the issue with using garnet rim compositions is that garnet porphyroclasts did not efficiently diffusively equilibrate with the matrix minerals. Instead, garnet was consumed, resulting in the redistribution of its components (primarily almandine) into the matrix, leading to more iron-rich biotite. The effect of disequilibrium between garnet and the matrix is best illustrated in GSL-18-C53, in which the garnet isopleths (pseudosection approach) predict peak metamorphism at ~0.8 GPa and ~725 ºC, whereas multi-phase thermobarometry (avPT) yielded a result of ~0.3 GPa and ~490 ºC. We consider the P–T results predicted by the pseudosection modelling for sample GSL-18-C53 to be more accurate than those predicted by avPT for two reasons. First, the pseudosection results are consistent with the observed mineral assemblages, notably the presence of sillimanite and melt (manifest as plagioclase–quartz–K-feldspar leucosome). Second, the thermal gradient from the pseudosection results (~900 ºC·GPa^{-1} as opposed to ~1625 ºC·GPa^{-1} for the avPT result), is consistent with the record of crustal thermal gradient preserved in the other GSLsz samples.

Based on the findings of this study, we have the following recommendations for quantifying P–T in crustal-scale shear zones. Equilibria modelling remains the most robust approach for determining the prograde and peak metamorphic conditions. When garnet is present, comparing measured compositions with modelled isopleths of pyrope and grossular is particularly useful for constraining peak conditions. However, in rocks in which garnet is chemically homogenized by intracrystalline diffusion and there is little control on the extent of equilibration between garnet and matrix phases, determining absolute prograde and peak P–T conditions remains challenging. Determining the final conditions of shear and recrystallization is more difficult. In samples with biotite-rich shear bands and folia, Ti-in-biotite thermometry appears to record the near-final

conditions of ductile shear. We found Ti-in-biotite temperatures to be systematically lower than those predicted by phase equilibria modelling. We believe this discrepancy to be the result of strain-induced recrystallization of biotite as strain was localized to biotite-rich shear plans during exhumation and cooling. In amphibole-bearing compositions, we found that amphibole–plagioclase thermometry provides reasonable and consistent estimates for matrix equilibrium. At amphibolite-facies conditions or lower, it is unlikely that significant diffusion would occur without recrystallization due to coupled Si-Al substitution in plagioclase (Grove, Baker, & Kinzler, 1984). As such, amphibole–plagioclase temperatures in sheared rocks are most likely to record the final temperature at which plagioclase dynamically recrystallized. In general, unless retrograde metamorphism was accompanied by thorough recrystallization (as with GSL-18-BD7), it is challenging to accurately model retrograde assemblages because the *effective* bulk composition is unknown for this portion of the rock's metamorphic history. As such, when determining the retrograde conditions, results from phase equilibria modelling should only be used as a general guide to the sequence and broad conditions of retrograde reactions.

We were fortunate to have access to paired mafic and pelitic samples from the upper- and epidote-amphibolite facies units. In both cases, complementary segments of the GSLsz metamorphic history were preserved in the different lithologies. Given the consistency of values generated by the independent thermometers, avPT, and pseudosection modelling for sample GSL-18-BD26, we have confidence in our results. However, there is a ~40 ºC difference in the peak-temperature recorded by GSL-18-BD26 (mafic) and the neighbouring GSL-18-BD25 (pelite). This discrepancy may be a consequence of using different datasets and activity-composition relations for the mafic and pelitic samples.

Finally, there is a wide range of independent single-phase thermometers that depend on the temperature-dependent substitution of minor or trace elements in metamorphic phases that may record additional information about the metamorphic evolution of shear zones. For example, Zr-in-rutile (Watson, Wark, & Thomas, 2006; Ferry & Watson, 2007) and Zr-in-titanite (Hayden, Watson, & Wark, 2008). When applying these thermometers to sheared rocks, it is important to assess whether or not the measured minerals recrystallized during shear. There are examples of titanite grains found in ductile shear zones that yield U–Pb ages that are associated with protolith crystallization rather than metamorphic recrystallization (Kohn & Corrie, 2011; Spencer et al., 2013). In these cases, if the isotopic systematics were not reset by shear (through the removal of incompatible Pb atoms), it seems unlikely that Zr would equilibrate with matrix phases and the Zr-in-titanite would reflect the temperature of shear. One thermometer that we did not use in this study that may be particularly useful for constraining the final temperatures of deformation in shear zones is the Ti-in-quartz thermometer of (Wark & Watson, 2006). While the Ti-in-quartz thermometer has its limitations (e.g., Kendrick & Indares, 2018), the application of Ti-in-quartz to the GSLsz rocks will be the subject of a follow-up study.

ACKNOWLEDGEMENTS

REFERENCES

Ashton, K. E., Hartlaub, R. P., Bethune, K. M., Heaman, L. M., Rayner, N., & Niebergall, G. R. (2013). New depositional age constraints for the Murmac Bay group of the southern Rae craton, Canada. *Precambrian Research*, *232*, 70–88. Elsevier.

Behr, W. M., & Platt, J. P. (2014). Brittle faults are weak, yet the ductile middle crust is strong: Implications for lithospheric mechanics. *Geophysical Research Letters*, *41*(22), 8067-8075.

Berman, R. G., Davis, W. J., Sanborn-Barrie, M., Whalen, J. B., Taylor, B. E., McMartin, I., McCurdy, M. W., et al. (2018). Report of activities for the GEM-2 Chantrey-Thelon activity: Thelon tectonic zone project, Nunavut. *Geological Survey of Canada, Open File 8372*, 22.

Berman, R. G., Pehrsson, S., Davis, W. J., Ryan, J. J., Qui, H., & Ashton, K. E. (2013). The Arrowsmith orogeny: Geochronological and thermobarometric constraints on its extent and tectonic setting in the Rae craton, with implications for pre-Nuna supercontinent reconstruction. *Precambrian Research*, *232*, 44–69. Elsevier.

Berman, R. G. (1991). Thermobarometry using multi-equilibrium calculations; a new technique, with petrological applications. *The Canadian Mineralogist*, *29*(4), 833–855.

Bethune, K. M., Berman, R. G., Rayner, N., & Ashton, K. E. (2013). Structural, petrological and U–Pb SHRIMP geochronological study of the western Beaverlodge domain: Implications for crustal architecture, multi-stage orogenesis and the extent of the Taltson orogen in the SW Rae craton, Canadian Shield. *Precambrian Research*, *232*, 89–118. Elsevier.

Bostock, H. H., & Loveridge, W. D. (1988). Geochronology of the Taltson magmatic zone and its eastern cratonic margin, District of Mackenzie. *Radiogenic age and isotopic studies: Report*, *2*, 90–2.

Bostock, H. H., Van Breemen, O., & Loveridge, W. D. (1987). Proterozoic geochronology in the Taltson magmatic zone, NWT. *Radiogenic age and isotopic studies: Report*, *1*, 87–1.

Bostock, H. H., Van Breemen, O., & Loveridge, W. D. (1991). Further geochronology of plutonic rocks in northern Taltson magmatic zone, District of Mackenzie, NWT. *Radiogenic age and isotopic studies, report 4*, 67–78. Geological Survey of Canada.

Bowring, S. A., Schmus, W. V., & Hoffman, P. F. (1984). U–Pb zircon ages from Athapuscow aulacogen, east arm of Great Slave Lake, NWT, Canada. *Canadian Journal of Earth Sciences*, *21*(11), 1315–1324. NRC Research Press.

Brown, M. (2007). Metamorphic conditions in orogenic belts: A record of secular change. *International Geology Review*, *49*(3), 193–234.

de Capitani, C., & Petrakakis, K. (2010). The computation of equilibrium assemblage diagrams with Theriak/Domino software. *American Mineralogist*, *95*(7), 1006–1016.

Card, C. D., Bethune, K. M., Davis, W. J., Rayner, N., & Ashton, K. E. (2014). The case for a distinct Taltson orogeny: Evidence from northwest Saskatchewan, Canada. *Precambrian Research*, *255*, 245–265.

Chacko, T., De, S. K., Creaser, R. A., & Muehlenbachs, K. (2000). Tectonic setting of the Taltson magmatic zone at 1.9 2.0 Ga: A granitoid-based perspective. *Canadian Journal of Earth Sciences*, *37*(11), 1597–1609.

Chatzaras, V., Tikoff, B., Newman, J., Withers, A. C., & Drury, M. R. (2015). Mantle strength of the San Andreas fault system and the role of mantle-crust feedbacks. *Geology*, *43*(10), 891-894.

Coggon, R., & Holland, T. J. B. (2002). Mixing properties of phengitic micas and revised garnet-phengite thermobarometers. *Journal of Metamorphic Geology*, *20*(7), 683–696.

Davis, W. J., Berman, R. G., & MacKinnon, A. (2013). U-Pb Geochronology of archival rock samples from the Queen Maud block, Thelon tectonic zone and Rae Craton, Kitikmeot Region, Nunavut, Canada. *Geological Survey of Canada, Open File 7409*.

Dyck, B., Waters, D. J., St-Onge, M. R., & Searle, M. P. (2019). Muscovite dehydration melting; reaction mechanisms, microstructures, and implications for anatexis. *Journal of Metamorphic Geology*.

England, P., & Thompson, A. B. (1984). Pressure—Temperature—Time paths of regional metamorphism I. Heat transfer during the evolution of regions of thickened continental crust. *Journal of Petrology*, *25*(4), 894–928.

Evans, T. P. (2004). A method for calculating effective bulk composition modification due to crystal fractionation in garnet-bearing schist: Implications for isopleth thermobarometry. *Journal of Metamorphic Geology*, *22*(6), 547–557.

Ferry, J. M., & Watson, E. B. (2007). New thermodynamic models and revised calibrations for the Ti-in-zircon and Zr-in-rutile thermometers. *Contributions to Mineralogy and Petrology*, *154*(4), 429–437.

Florence, F. P., & Spear, F. S. (1995). Intergranular diffusion kinetics of Fe and Mg during retrograde metamorphism of a pelitic gneiss from the Adirondack Mountains. *Earth and Planetary Science Letters*, *134*(3–4), 329–340.

Forshaw, J. B., Waters, D. J., Pattison, D. R., Palin, R. M., & Gopon, P. (2019). A comparison of observed and thermodynamically predicted phase equilibria and mineral compositions in mafic granulites. *Journal of Metamorphic Geology*, *37*(2), 153–179.

Gibb, R. A. (1978). Slave–Churchill collision tectonics. *Nature*, *271*(5640), 50–52. Springer.

Green, E. C. R., White, R. W., Diener, J. F. A., Powell, R., Holland, T. J. B., & Palin, R. M. (2016). Activity–composition relations for the calculation of partial melting equilibria in metabasic rocks. *Journal of Metamorphic Geology*, *34*(9), 845–869.

Grove, T. L., Baker, M. B., & Kinzler, R. J. (1984). Coupled CaAl-NaSi diffusion in plagioclase feldspar: Experiments and applications to cooling rate speedometry. *Geochimica et Cosmochimica Acta*, *48*(10), 2113–2121.

Gottlieb, P., Wilkie, G., Sutherland, D., Ho-Tun, E., Suthers, S., Perera, K., B., Jenkins, S., Spencer, A. Butcher, & Rayner, J. (2000). Using quantitative electron microscopy for process mineralogy applications. *Jom*, *52*(4), 24-25.

Hanmer, S. (1988). Great Slave Lake Shear Zone, Canadian Shield: Reconstructed vertical profile of a crustal-scale fault zone. *Tectonophysics*, *149*(3), 245–264.

Hanmer, S. (1997). Shear zone reactivation at granulite facies: The importance of plutons in the localization of viscous flow. *Journal of the Geological Society*, *154*(1), 111–116.

Hanmer, S., Bowring, S., van Breemen, O., & Parrish, R. (1992). Great Slave Lake shear zone, NW Canada: Mylonitic record of Early Proterozoic continental convergence, collision and indentation. *Journal of Structural Geology*, *14*(7), 757–773.

Hanmer, S., & Lucas, S. B. (1985). Anatomy of a ductile transcurrent shear: The Great Slave Lake Shear Zone, District of Mackenzie, NWT (preliminary report). *Geol. Surv. Pap. Can*, 7–22.

Hartlaub, R. P., Heaman, L. M., Chacko, T., & Ashton, K. E. (2007). Circa 2.3-Ga magmatism of the Arrowsmith orogeny, Uranium City region, western Churchill craton, Canada. *The Journal of Geology*, *115*(2), 181–195. The University of Chicago Press.

Hayden, L. A., Watson, E. B., & Wark, D. A. (2008). A thermobarometer for sphene (titanite). *Contributions to Mineralogy and Petrology*, *155*(4), 529–540.

Henderson, J. B., & Loveridge, W. D. (1990). Inherited Archean zircon in the Proterozoic Thelon Tectonic Zone: U-Pb geochronology of the Campbell granite, south of McDonald fault, District of Mackenzie, Northwest Territories. *Geol. Surv. Can. Pap.*, *89*, 63–70.

Henry, D. J., Guidotti, C. V., & Thomson, J. A. (2005). The Ti-saturation surface for low-to-medium pressure metapelitic biotites: Implications for geothermometry and Ti-substitution mechanisms. *American Mineralogist*, *90*(2–3), 316–328.

Hoffman, P. F. (1987). Continental transform tectonics: Great Slave Lake shear zone (ca. 1.9 Ga), northwest Canada. *Geology*, *15*(9), 785–788.

Holdsworth, R. E., Butler, C. A., & Roberts, A. M. (1997). The recognition of reactivation during continental deformation. *Journal of the Geological Society*, *154*(1), 73–78.

Holdsworth, R. E., Stewart, M., Imber, J., & Strachan, R. A. (2001). The structure and rheological evolution of reactivated continental fault zones: A review and case study. *Geological Society, London, Special Publications*, *184*(1), 115–137.

Holdsworth, R. E. (2004). Weak Faults—Rotten Cores. *Science*, *303*(5655), 181–182.

Holland, T. J. B., & Blundy, J. (1994). Non-ideal interactions in calcic amphiboles and their bearing on amphibole-plagioclase thermometry. *Contributions to mineralogy and petrology*, *116*(4), 433–447.

Holland, T. J. B. (2018). AX62: A program to calculate activities of mineral end-members from chemical analyses.

Holland, T. J. B., & Powell, R. (1998). An internally consistent thermodynamic data set for phases of petrological interest. *Journal of Metamorphic Geology*, *16*(3), 309–343.

Holland, T. J. B., & Powell, R. (2009). AX: A program to calculate activities of mineral end-members from chemical analyses. *Last accessed*, *12*, 2014.

Holland, T. J. B., & Powell, R. (2003). Activity–composition relations for phases in petrological calculations: An asymmetric multicomponent formulation. *Contributions to Mineralogy and Petrology*, *145*(4), 492–501.

Holland, T. J. B., & Powell, R. (2011). An improved and extended internally consistent thermodynamic dataset for phases of petrological interest, involving a new equation of state for solids: Thermodynamics dataset for phases of petrological interest. *Journal of Metamorphic Geology*, *29*(3), 333–383.

Imber, J., Holdsworth, R. E., Smith, S. A. F., Jefferies, S. P., & Collettini, C. (2008). Frictional-viscous flow, seismicity and the geology of weak faults: A review and future directions. *Geological Society, London, Special Publications*, *299*(1), 151–173. Geological Society of London.

Jefferies, S. P., Holdsworth, R. E., Wibberley, C. A. J., Shimamoto, T., Spiers, C. J., Niemeijer, A. R., & Lloyd, G. E. (2006). The nature and importance of phyllonite development in crustal-scale fault cores: An example from the Median Tectonic Line, Japan. *Journal of Structural Geology*, *28*(2), 220–235.

Kendrick, J., & Indares, A. (2018). The Ti record of quartz in anatectic aluminous granulites. *Journal of Petrology*, *59*(8), 1493-1516.

Kohn, M. J., & Corrie, S. L. (2011). Preserved Zr-temperatures and U–Pb ages in high-grade metamorphic titanite: Evidence for a static hot channel in the Himalayan orogen. *Earth and Planetary Science Letters*, *311*(1–2), 136–143.

Kohn, M. J., & Spear, F. (2000). Retrograde net transfer reaction insurance for pressure-temperature estimates. *Geology*, *28*(12), 1127–1130.

Konrad-Schmolke, M., O'Brien, P. J., de Capitani, C., & Carswell, D. A. (2008). Garnet growth at high- and ultra-high pressure conditions and the effect of element fractionation on mineral modes and composition. *Lithos*, *103*(3), 309–332.

Koons, P. O., Rubie, D. C., & Fruch-Green, G. (1987). The effects of disequilibrium and deformation on the mineralogical evolution of quartz diorite during metamorphism in the eclogite facies. *Journal of Petrology*, *28*(4), 679–700.

Leake, B. E., Woolley, A. R., Birch, W. D., Burke, E. a. J., Ferraris, G., Grice, J. D., Hawthorne, F. C., et al. (2004). Nomenclature of amphiboles: Additions and revisions to the International Mineralogical Association's amphibole nomenclature. *Mineralogical Magazine*, *68*(1), 209–215.

Leake, B. E., Wooley, A. R., Arps, C. E. S., Birch, W. D., Gilbert, M. C., Grice, J. D., Hawthorne, F. C., et al. (1997). Nomenclature of amphiboles; report of the Subcommittee on Amphiboles of the International Mineralogical Association Commission on New Minerals and Mineral Names. *European Journal of Mineralogy*, *9*(3), 623–651.

Ma, S. M., Kellett, D. A.-M., Godin, L., & Jercinovic, M. (2019). Localisation of the brittle Bathurst fault on pre-existing fabrics: A case for structural inheritance in the northeastern

Slave craton, western Nunavut, Canada. *Canadian Journal of Earth Sciences*, (ja). NRC Research Press.

Marsh, J. H., Johnson, S. E., Yates, M. G., & West, D. P. (2009). Coupling of deformation and reactions during mid-crustal shear zone development: An in situ frictional–viscous transition. *Journal of Metamorphic Geology*, *27*(8), 531–553.

McDonough, M. R., McNicoll, V. J., Schetselaar, E. M., & Grover, T. W. (2000). Geochronological and kinematic constraints on crustal shortening and escape in a two-sided oblique-slip collisional and magmatic orogen, Paleoproterozoic Taltson magmatic zone, northeastern Alberta. *Canadian Journal of Earth Sciences*, *37*(11), 1549–1573. NRC Research Press.

McNicoll, V. J., Thériault, R. J., & McDonough, M. R. (2000). Taltson basement gneissic rocks: U Pb and Nd isotopic constraints on the basement to the Paleoproterozoic Taltson magmatic zone, northeastern Alberta. *Canadian Journal of Earth Sciences*, *37*(11), 1575–1596. NRC Research Press.

Miles, W., & Oneschuck, D. (2016). Magnetic Anomaly Mao, Canada / Carte des anomalies magnetiques, Canada. *Geological Survey of Canada, Open File 7799*.

Miller, A. R., Cumming, G. L., & Krstic, D. (1989). U–Pb, Pb–Pb, and K–Ar isotopic study and petrography of uraniferous phosphate-bearing rocks in the Thelon Formation, Dubawnt Group, Northwest Territories, Canada. *Canadian Journal of Earth Sciences*, *26*(5), 867–880. NRC Research Press.

Nabelek, P. I., Whittington, A. G., & Hofmeister, A. M. (2010). Strain heating as a mechanism for partial melting and ultrahigh temperature metamorphism in convergent orogens:

Implications of temperature-dependent thermal diffusivity and rheology. *Journal of Geophysical Research: Solid Earth*, *115*(B12).

Norris, R. J., & Toy, V. G. (2014). Continental transforms: A view from the Alpine Fault. *Journal of Structural Geology*, *64*, 3–31. Elsevier.

Palin, R. M., Weller, O. M., Waters, D. J., & Dyck, B. (2016). Quantifying geological uncertainty in metamorphic phase equilibria modelling; a Monte Carlo assessment and implications for tectonic interpretations. *Geoscience Frontiers*, *7*(4), 591–607.

Parsons, A. J., Law, R. D., Lloyd, G. E., Phillips, R. J., & Searle, M. P. (2016). Thermo-kinematic evolution of the Annapurna-Dhaulagiri Himalaya, central Nepal: The Composite Orogenic System. *Geochemistry, Geophysics, Geosystems*, *17*(4), 1511–1539.

Phillips, R. J., & Searle, M. P. (2007). Macrostructural and microstructural architecture of the Karakoram fault: Relationship between magmatism and strike-slip faulting. *Tectonics*, *26*(3). Wiley Online Library.

Pouchou, J. L., & Pichoir, F. (1985). PAP $\phi(\rho Z)$ procedure for improved quantitative microanalysis. *Microbeam Analysis*, 104–106.

Powell, R., & Holland, T. J. B. (2008). On thermobarometry. *Journal of Metamorphic Geology*, *26*(2), 155–179.

Powell, R., & Holland, T. J. B. (1994). Optimal geothermometry and geobarometry. *American Mineralogist*, *79*(1–2), 120–133.

Scholz, C. H. (1988). The brittle-plastic transition and the depth of seismic faulting. *Geologische Rundschau*, *77*(1), 319–328.

Schultz, M. E., Chacko, T., Heaman, L. M., Sandeman, H. A., Simonetti, A., & Creaser, R. A. (2007). Queen Maud block: A newly recognized Paleoproterozoic (2.4–2.5 Ga) terrane in northwest Laurentia. *Geology*, *35*(8), 707–710.

Sheen, A. I., Heaman, L. M., Kjarsgaard, B., Ootes, L., Pearson, D. G., & Creaser, R. A. (2019). Athapuscow aulacogen revisited: Geochronology and geochemistry of the 2046 Ma Union Island Group mafic magmatism, East Arm of Great Slave Lake, Northwest Territories, Canada. *Precambrian Research*, *321*, 85–102.

Sibson, R. H. (1977). Fault rocks and fault mechanisms. *Journal of the Geological Society*, *133*(3), 191–213.

Sibson, R. H. (1983). Continental fault structure and the shallow earthquake source. *Journal of the Geological Society*, *140*(5), 741–767.

Spear, F. S., & Selverstone, J. (1983). Quantitative PT paths from zoned minerals: Theory and tectonic applications. *Contributions to Mineralogy and Petrology*, *83*(3–4), 348–357.

Spencer, K. J., Hacker, B. R., Kylander-Clark, A. R. C., Andersen, T. B., Cottle, J. M., Stearns, M. A., Poletti, J. E., et al. (2013). Campaign-style titanite U–Pb dating by laser-ablation ICP: Implications for crustal flow, phase transformations and titanite closure. *Chemical Geology*, *341*, 84–101.

Starr, P. G., Pattison, D. R. M., & Ames, D. E. (2020). Mineral assemblages and phase equilibria of metabasites from the prehnite–pumpellyite to amphibolite facies, with the Flin Flon Greenstone Belt (Manitoba) as a type example. *Journal of Metamorphic Geology*, *38*(1), 71–102.

St-Onge, M. R. (1987). Zoned poikiloblastic garnets: PT paths and syn-metamorphic uplift through 30 km of structural depth, Wopmay Orogen, Canada. *Journal of Petrology*, *28*(1), 1–21.

Tersmette, D. B. (2012). Geology, geochronology, thermobarometry, and tectonic evolution of the Queen Maud block, Churchill craton, Nunavut, Canada.

Thatcher, W., & England, P. C. (1998). Ductile shear zones beneath strike-slip faults: Implications for the thermomechanics of the San Andreas Fault zone. *Journal of Geophysical Research: Solid Earth*, *103*(B1), 891-905.

Thériault, R. J. (1992). Nd isotopic evolution of the Taltson magmatic zone, Northwest Territories, Canada: Insights into Early Proterozoic accretion along the western margin of the Churchill Province. *The Journal of Geology*, *100*(4), 465–475.

Thiessen, E. J., Gibson, H. D., Regis, D., Pehrsson, S. J., Cutts, J. A., & Smit, M. A. (2019). High-grade metamorphism flying under the radar of accessory minerals. *Geology*, *47*(6), 568–572.

Tinkham, D. K., & Ghent, E. D. (2005). Estimating PT conditions of garnet growth with isochemical phase-diagram sections and the problem of effective bulk-composition. *The Canadian Mineralogist*, *43*(1), 35–50.

Toy, V. G., Prior, D. J., & Norris, R. J. (2008). Quartz fabrics in the Alpine Fault mylonites: Influence of pre-existing preferred orientations on fabric development during progressive uplift. *Journal of Structural Geology*, *30*(5), 602–621. Elsevier.

Tracy, R. J. (1982). Compositional zoning and inclusions in metamorphic minerals. *Characterization of Metamorphism through Mineral Equilibria, Review in Mineralogy*, 355–397.

Wallis, D., Phillips, R. J., & Lloyd, G. E. (2013). Fault weakening across the frictional-viscous transition zone, Karakoram Fault Zone, NW Himalaya. *Tectonics*, *32*(5), 1227–1246. Wiley Online Library.

Wark, D. A., & Watson, E. B. (2006). TitaniQ: A titanium-in-quartz geothermometer. *Contributions to Mineralogy and Petrology*, *152*(6), 743–754.

Waters, D. J. (2019). Metamorphic constraints on the tectonic evolution of the High Himalaya in Nepal: The art of the possible. *Geological Society, London, Special Publications*, *483*, SP483-2018–187.

Watson, E. B., Wark, D. A., & Thomas, J. B. (2006). Crystallization thermometers for zircon and rutile. *Contributions to Mineralogy and Petrology*, *151*(4), 413.

Weller, O. M., Copley, A., Miller, W. G. R., Palin, R. M., & Dyck, B. (2019). The relationship between mantle potential temperature and oceanic lithosphere buoyancy. *Earth and Planetary Science Letters*, *518*, 86–99.

Weller, O. M., St-Onge, M. R., Waters, D. J., Rayner, N., Searle, M. P., Chung, S.-L., Palin, R. M., et al. (2013). Quantifying Barrovian metamorphism in the Danba structural culmination of eastern Tibet. *Journal of Metamorphic Geology*, *31*(9), 909–935.

Whalen, J. B., Berman, R. G., Davis, W. J., Sanborn-Barrie, M., & Nadeau, L. (2018). *Bedrock geochemistry of the central Thelon tectonic zone, Nunavut*. Geological Survey of Canada.

White, R. W., Powell, R., & Clarke, G. L. (2002). The interpretation of reaction textures in Fe-rich metapelitic granulites of the Musgrave Block, central Australia: Constraints from mineral equilibria calculations in the system K2O–FeO–MgO–Al2O3–SiO2–H2O–TiO2–Fe2O3. *Journal of Metamorphic Geology*, *20*(1), 41–55.

White, R. W., Powell, R., & Holland, T. J. B. (2007). Progress relating to calculation of partial

melting equilibria for metapelites. *Journal of Metamorphic Geology*, *25*(5), 511–527.

White, R. W., Powell, R., Holland, T. J. B., Johnson, T. E., & Green, E. C. R. (2014). New

mineral activity–composition relations for thermodynamic calculations in metapelitic

systems. *Journal of Metamorphic Geology*, *32*(3), 261–286.

White, R. W., Powell, R., Holland, T. J. B., & Worley, B. A. (2000). The effect of TiO2 and

Fe2O3 on metapelitic assemblages at greenschist and amphibolite facies conditions:

Mineral equilibria calculations in the system K2O-FeO-MgO-Al2O3-SiO2-H2O-TiO2-

Fe2O3. *Journal of Metamorphic Geology*, *18*(5), 497–511.

Xiao, W. J., Windley, B. F., Liu, D. Y., Jian, P., Liu, C. Z., Yuan, C., & Sun, M. (2005).

Accretionary tectonics of the Western Kunlun Orogen, China: A Paleozoic–Early

Mesozoic, long-lived active continental margin with implications for the growth of

Southern Eurasia. *The Journal of Geology*, *113*(6), 687–705. The University of Chicago

Press.

TABLES

Sample ID	Quartz	K-Feldspar	Altered Albite	Albite	Plagioclase	White mica (r)	Biotite	Chlorite (r)	Amphibole	Garnet	Sillimanite	Epidote/ Zoisite	Calcite	Fe Sulphides	Rutile & Ilmenite	Titanite	Apatite
GSL-18-BD07	11.6	5.2	17.6	9.4	15.7	6.6	1.5	4.2	25.0	0.0	0.0	0.9	0.2	0.0	0.0	1.4	0.4
GSL-18-BD25	36.3	11.6	6.3	7.4	4.2	15.3	13.8	1.6	0.0	2.4	0.8	0.0	0.0	0.0	0.0	0.0	0.1
GSL-18-BD26	10.2	0.2	2.6	0.3	19.2	3.8	0.6	1.2	55.8	3.9	0.0	0.4	0.1	0.1	0.9	0.2	0.3
GSL-18-C47	26.0	8.8	1.8	0.6	27.7	2.8	11.9	0.6	0.1	7.7	10.5	0.0	0.1	0.1	0.1	0.1	0.0
GSL-18-C50	26.6	13.3	2.1	1.1	0.6	9.5	2.5	6.0	11.6	0.0	0.0	20.9	0.7	0.6	0.0	2.6	0.4
GSL-18-C53	23.7	4.0	6.8	3.4	12.7	14.4	13.6	7.7	0.6	11.4	0.5	0.0	0.1	0.2	0.1	0.1	0.3

Table 1. Mineral modes obtained by automated mineralogical mapping of thin-sections.

Table 2. Representative mineral compositions (wt.% oxide and cations per formula unit) for samples used in this study. Available upon request (brendan_dyck[at]sfu.ca)

Sample	Metamorphic Grade	Composition	Figure	$P_{saturation}$ (GPa)§	H_2O	SiO_2	Al_2O_3	CaO	MgO	FeO	Fe_2O_3	K_2O	Na_2O	TiO_2	MnO	XMg	XFe³⁺
GSL-18-BD07	Greenshist	Granodiorite	Fig. 10		20.00	51.89	6.92	6.31	5.97	3.55	0.08	0.50	3.31	1.33	0.00	0.62	0.04
GSL-18-C50	Lower Amph.	Diorite	Fig. 9b	0.7	2.60	58.43	6.83	7.78	2.34	5.30	0.99	1.20	1.58	3.57	0.00	0.24	0.27
GSL-18-C53	Lower Amph.	Pelite	Fig. 9a	0.7	20.00	50.83	9.40	3.45	3.54	7.68	0.19	1.20	1.99	1.11	0.22	0.30	0.05
GSL-18-C53	Grt core removed		Fig. 9a	0.7	2.60	52.16	9.28	3.20	3.63	6.52	0.17	1.30	2.15	1.19	0.06	0.35	0.05
GSL-18-BD25	Upper Amph.	Pelite	Fig. 8a	0.7	3.60	58.77	7.16	0.98	2.77	3.44	0.14	1.91	2.14	2.37	0.04	0.43	0.07
GSL-18-BD26	Upper Amph.	Basalt	Fig. 8b	0.7	2.60	48.97	4.94	8.88	7.53	6.54	0.43	0.03	1.72	0.03	0.07	0.50	0.12
GSL-18-C47	Granulite	Pelite	Fig. 7	0.7	2.90	53.36	11.33	2.61	2.38	4.39	0.18	1.89	1.97	0.08	0.18	0.33	0.08

Table 3. Bulk-rock compositions used to construct phase diagrams (mole % oxide). Bulk-rock Xmg = MgO/(MgO + FeO + Fe_2O_3*2). XFe³⁺ = (Fe_2O_3*2)/(Fe_2O_3*2 + FeO). § Pressure at which H_2O minimally saturates the solidus.

FIGURES
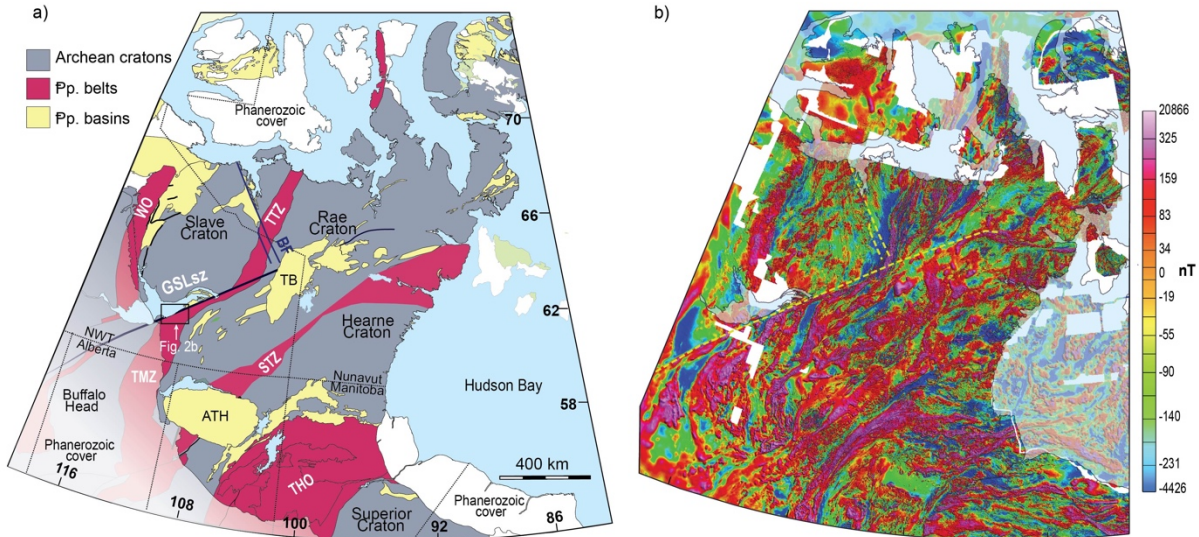
Figure 1. Regional maps. a) Bedrock map for northern Laurentia presenting the locations of the Great Slave Lake shear zone (GSLsz) and conjugate Bathurst Fault (BF). Paleoproterozoic belts:

TMZ – Taltson Magmatic zone, TTZ – Thelon Tectonic Zone, WO – Wopmay Orogen, STZ – Snowbird Tectonic Zone, THO – Trans Hudson Orogen. Paleoproterozoic basins: TB – Thelon Basin, ATH – Athabasca Basin. Modified after Ashton et al. (2013) and Thiessen et al. (2019). b) Aeromagnetic map modified after Miles and Oneschuck (2016).
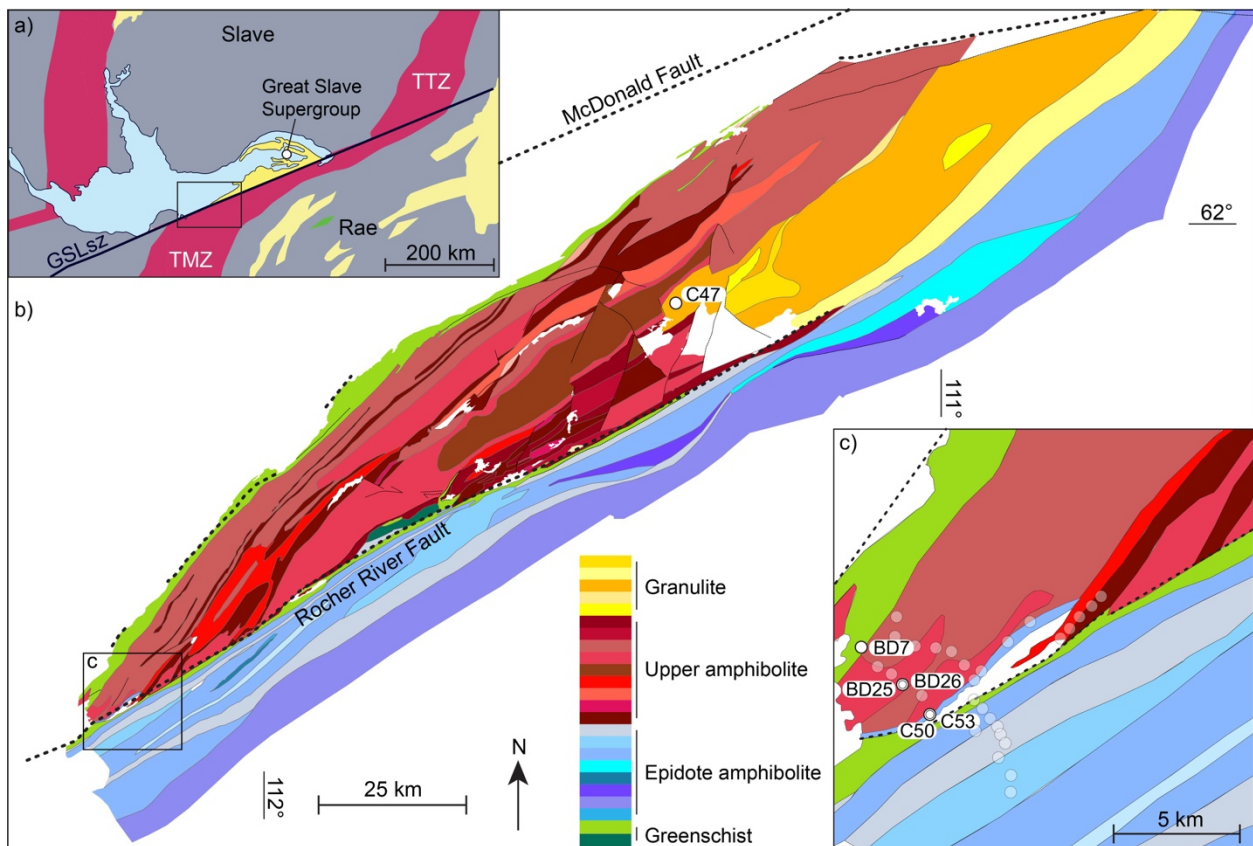

Figure 2. a) Inset indicating the location of our study area relative to the Slave–Rae boundary. b) Map of metamorphic grades for the southwestern exposure of the Great Slave Lake shear zone. Shading corresponds to the protolith lithology as mapped by Hanmer (1988). c) Close-up of the southwestern study area with the location of the samples collected for this study marked by white circles. The samples that were selected for petrological modelling are labelled on frames (b) and (c).
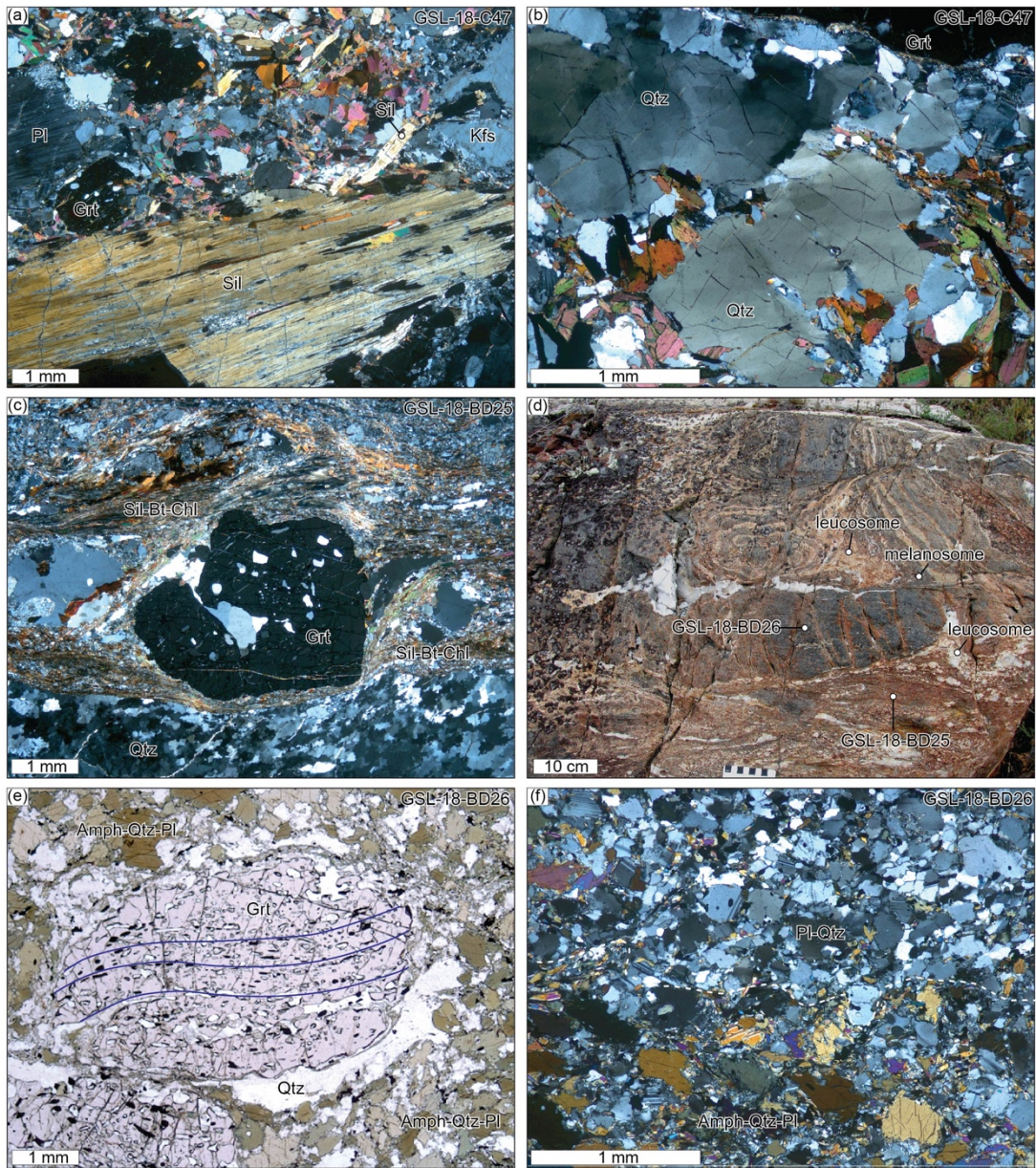
Figure 3. Petrological features in granulite and upper-amphibolite facies units. (a) Sillimanite–quartz pseudomorph after kyanite surrounded by matrix of plagioclase–K-feldspar–biotite (GSL-18-C47). (b) Checkboard microstructure in quartz (GSL-18-C47). (c) Garnet porphyroclast in sample GSL-18-BD25 surrounded by polycrystalline quartz and sillimanite–biotite folia. (d) Intercalation of garnet-amphibolite (GSL-18-BD26) and sillimanite–garnet schist (GSL-18-

BD25). (e) Garnet porphyroblast with sigmoidal quartz–ilmenite inclusion trails (GSL-18-BD26). (f) Leucosome containing plagioclase and quartz (above dashed line; GSL-18-BD26).
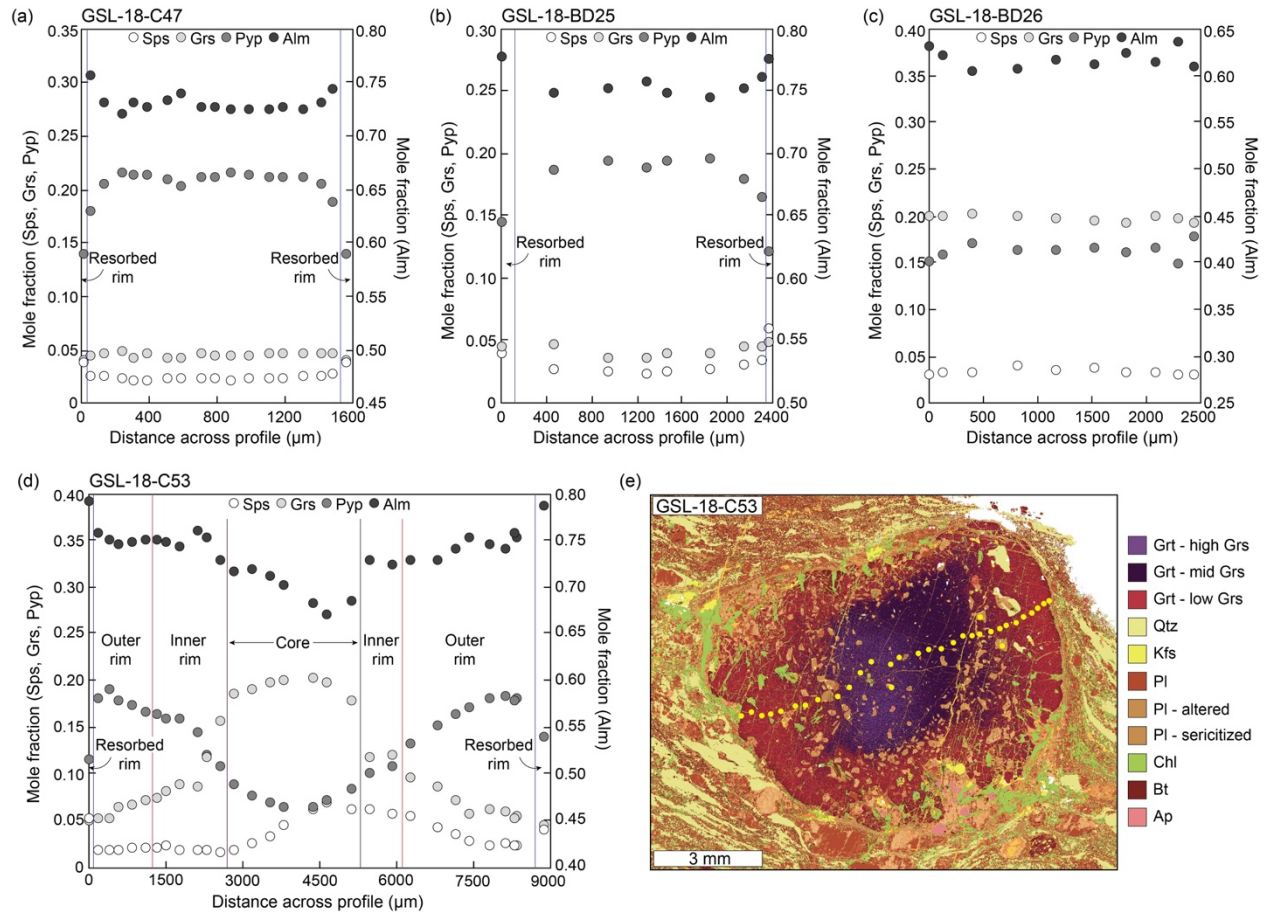
Figure 4. Garnet compositional line profiles. (a–d) Rim-to-rim profiles of garnet end-member mole fractions for GSL-18-C47, GSL-18-BD25, GSL-18-BD26, and GSL-18-C53. (e) Phase map of a garnet porphyroblast from sample GSL-18-C53 with prograde growth zoning. Location of probe points marked by yellow circles.
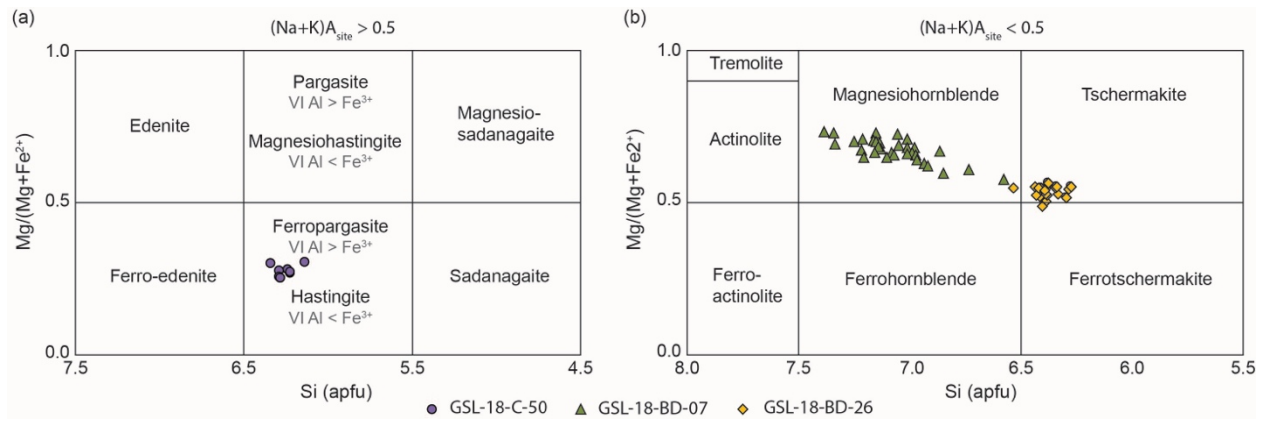
Figure 5. Amphibole classification plots (after Leake et al., 1997, 2004) in terms of Si atoms per formula unit and Mg/(Fe^{2+} + Mg). (a) Group 2 calcic amphiboles with Na + K on the A site > 0.5. (b) Group 2 calcic amphiboles with Na + K on the A site < 0.5.
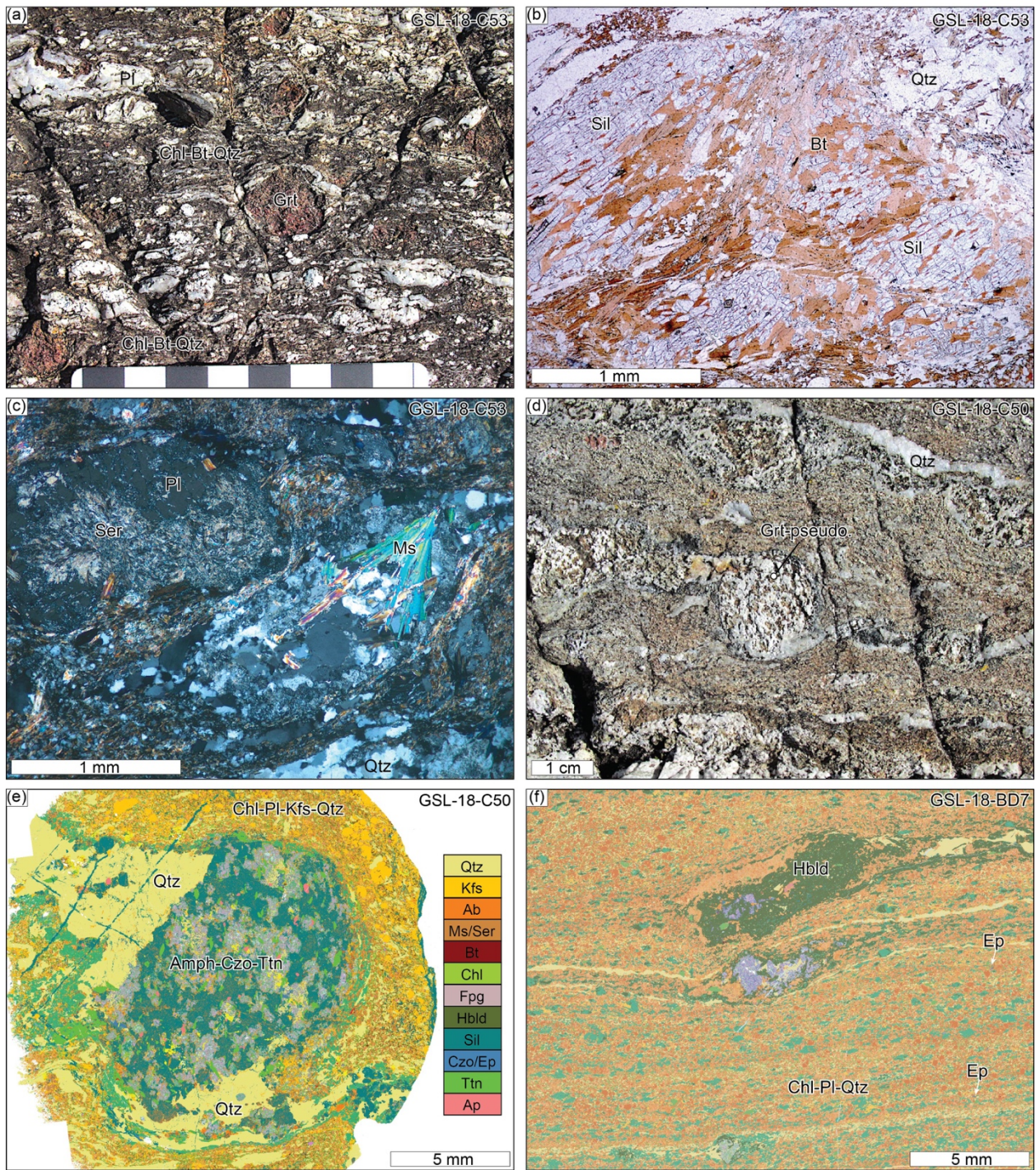
Figure 6. Petrological features in epidote-amphibolite and greenschist facies units. (a)
Porphyroclasts of garnet, plagioclase and K-feldspar surrounded by matrix of chlorite–biotite–
quartz (GSL-18-C53). (b) Intergrowth of prismatic sillimanite and biotite (GSL-18-C53). (c)

White mica alteration of plagioclase (GSL-18-C53). (d) Garnet-shaped porphyroclast with quartz strain shadows (GSL-18-C50). (e) Phase map showing an intergrowth of amphibole(ferropargasite)–clinozoisite–titanite surrounded by matrix of chlorite–plagioclase–K-feldspar–quartz (GSL-18-C50). (f) Phase map of GSL-18-BD7 depicting compositional layering. Note phase colour key is the same as frame (e).
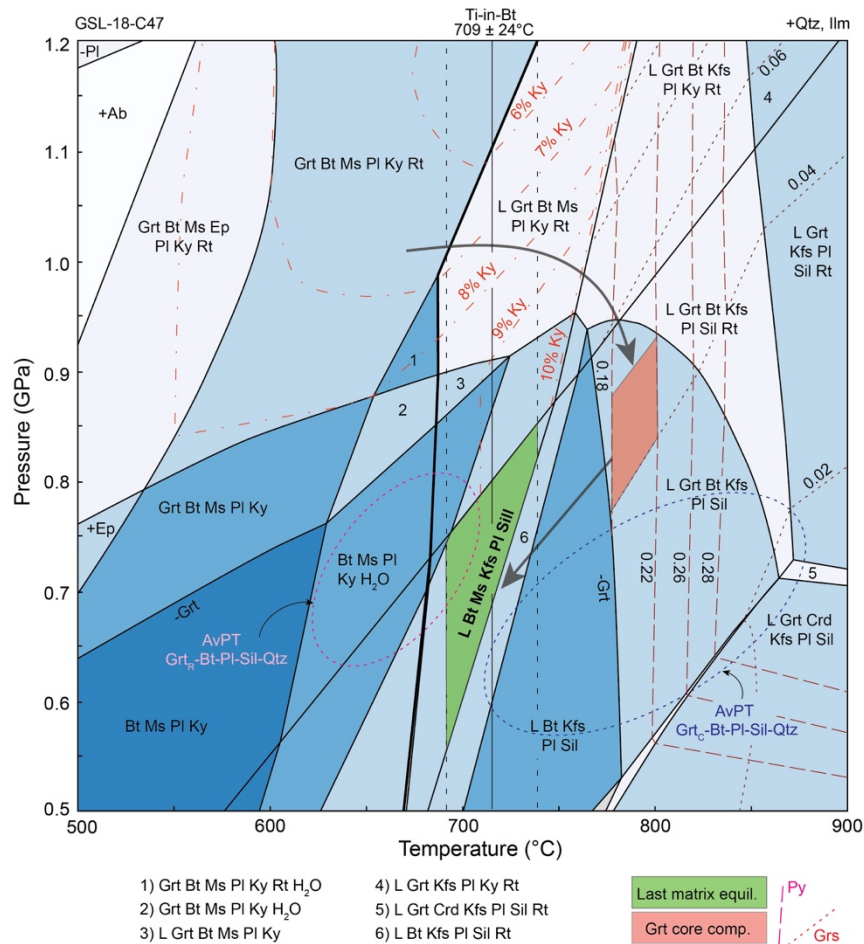
Figure 7. Calculated *P–T* pseudosection for sample GSL-18-C47. Relevant fields are contoured for pyrope and grossular isopleths and kyanite mode (legend, bottom right). Red polygon represents the garnet core composition (±10% of end-member mole fraction). The diagram is overlain by Ti-in-biotite temperature and avPT error ellipses (1 S.D.) for calculations including

garnet core and rim compositions. The green polygon represents the range of conditions in which the Ti-in-biotite temperatures overlap with the observed stable mineral assemblage (bold text).
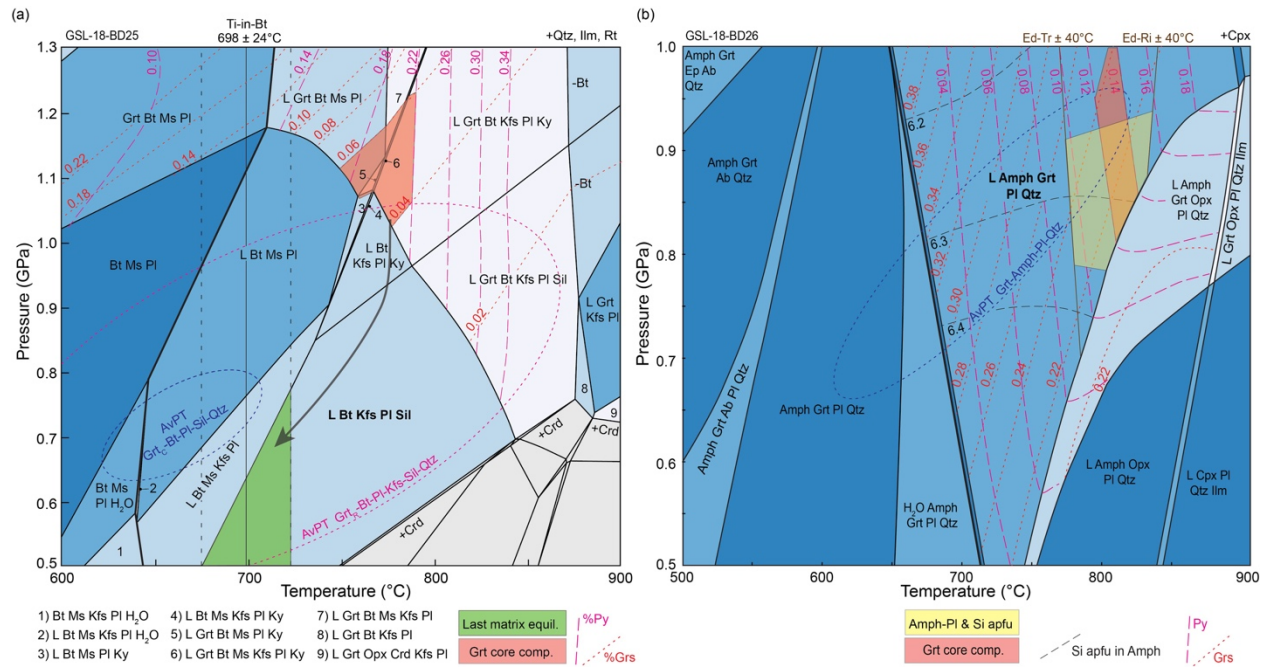

Figure 8. Calculated *P–T* pseudosection for samples (a) GSL-18-BD25, and (b) GSL-18-BD26. Note pressure range differs between pseudosections. In both diagrams, relevant fields are contoured for pyrope and grossular isopleths and Si apfu in amphibole (legend, below each diagram). Bold text marks the observed stable mineral assemblage. Red polygons represent the garnet core composition (±10% of end-member mole fraction). Diagram (a) is overlain by Ti-in-biotite temperature and avPT error ellipses (1 S.D.). The green polygon represents the range of conditions in which thermobarometry estimates overlap with a peritectic K-feldspar-bearing field. Diagram (b) is overlain by the results of the Holland & Blundy (1994) amphibole–plagioclase thermometers and avPT calculation (1 S.D.). The yellow polygon represents the range of conditions in which the observed amphibole composition is bracketed by amphibole–plagioclase thermometry results.
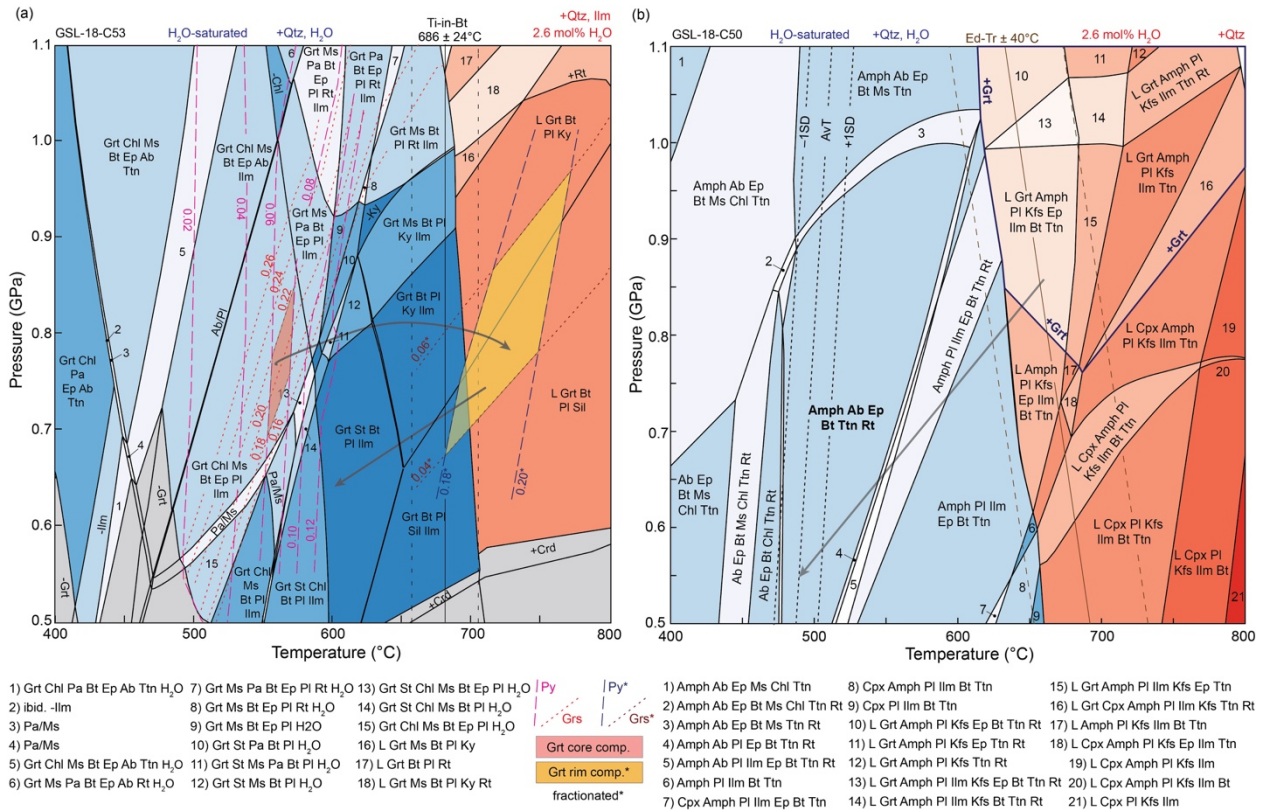
Figure 9. Calculated *P–T* pseudosection for samples (a) GSL-18-C53, and (b) GSL-18-C50. Bold text marks the observed mineral assemblage. (a) Pyrope and grossular isopleths are overlain in relevant fields for both the unfractionated bulk composition and a fractionated composition with garnet core removed. The red polygon represents the garnet core composition (±10% of end-member mole fraction), whereas the green polygon represents the conditions in which garnet rim equilibrated. Diagram is overlain by Ti-in-biotite temperature. (b) Sub-solidus assemblage fields calculated with excess H_2O (blue fields), supra-solidus assemblage fields calculated with minimal H_2O-saturation (red fields). Garnet is stable within the bolded blue polygon. Diagram (b) is overlain by results of edenite–tremolite thermometer and avT calculation (with 1 S.D. errors).
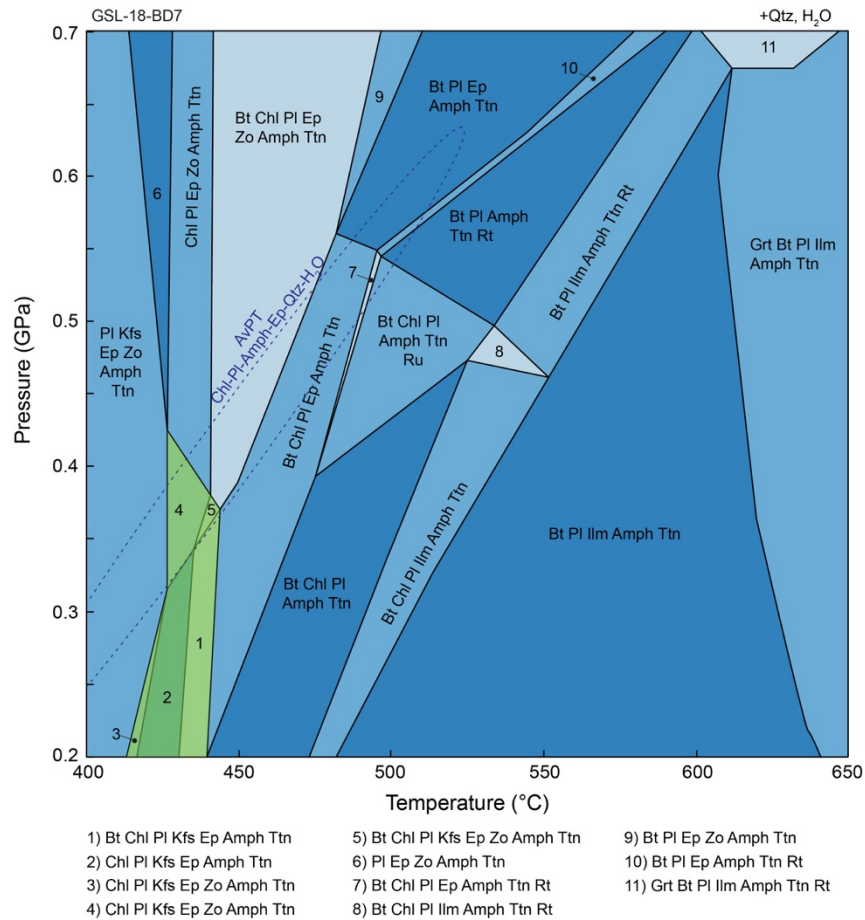
Figure 10. Calculated *P–T* pseudosection for sample GSL-18-BD7. The green polygon

represents the predicted stability field for the observed mineral assemblage chlorite–plagioclase–

epidote(±zoisite)–amphibole–titanite±biotite. Diagram overlain by avPT error ellipse (1 S.D.).
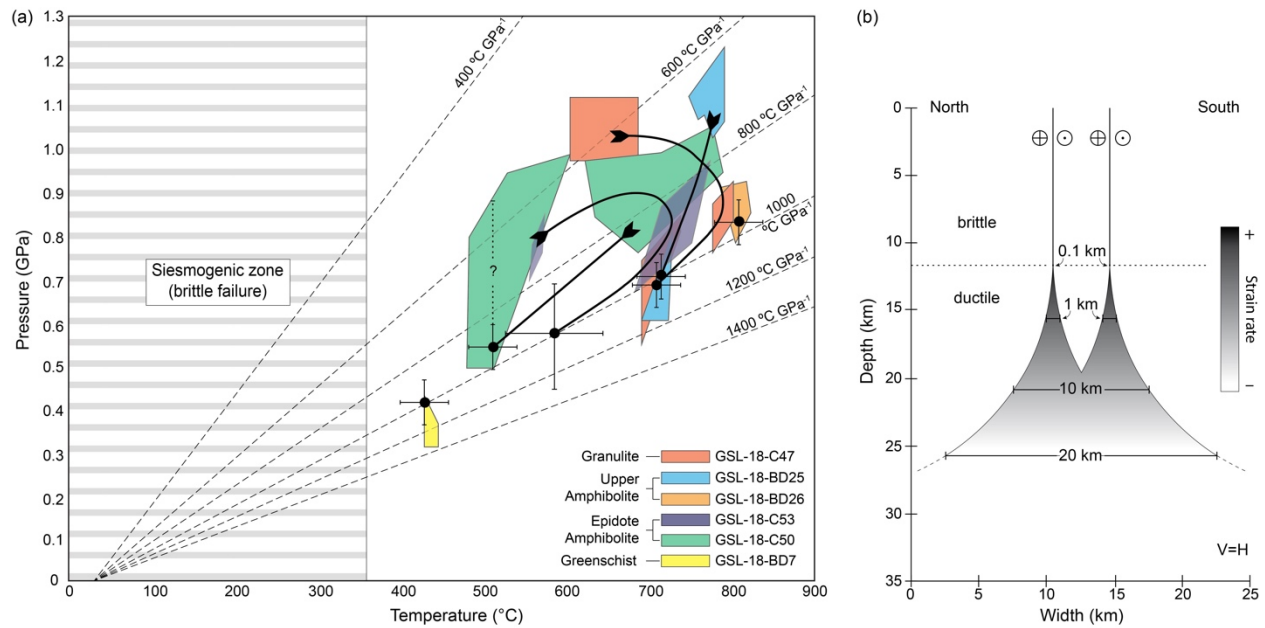
Figure 11. (a) Summary of all *P–T* results reported in this study. Black circles represent the best estimates for the last recorded equilibrium conditions (with 1 S.D. error bars). Linear geotherms (dashed lines) intercept the surface at 25 ºC. The results suggest crustal thickening and Barrovian-style prograde metamorphism progressed under a geotherm of ~600 ºC·GPa^{-1}. The last recorded equilibrium conditions yield a metamorphic field gradient of ~1000 ºC·GPa^{-1}. (b) Schematic cross-section of the GSLsz. Shear zone width is based on surface geology with the depth of each unit calculated assuming an average overburden density of 2750 kg·m^{-3}.

SUPPORTING INFORMATION